Petroleum Science 23 (2026) 2288–2307

Contents lists available at ScienceDirect

Petroleum Science

journal homepage: www.keaipublishing.com/en/journals/petroleum-science

Original Paper

An integrated deep learning framework for full-cycle CCUS-EOR evaluation and optimization under carbon neutrality

Bin Shen [a,b,c], Sheng-Lai Yang [a,b,*], Yi-Qi Zhang [b], Xin-Yuan Gao [b], Lu-Fei Bi [b], Kai Du [b], Er-Meng Zhao [d], Hong-Bo Zeng [c,**]

[a] College of Artificial Intelligence, China University of Petroleum (Beijing), Beijing, 102249, China
[b] State Key Laboratory of Petroleum Resources and Prospecting, China University of Petroleum (Beijing), Beijing, 102249, China
[c] Donadeo Innovation Centre for Engineering, University of Alberta, Edmonton, T6G 1H9, Canada
[d] School of Energy Resources, China University of Geosciences, Beijing, 100083, China

ARTICLE INFO

Article history:
Received 11 June 2025
Received in revised form
1 November 2025
Accepted 19 January 2026
Available online 27 January 2026

Edited by Min Li

Keywords:
CCUS-EOR
CO_2 storage
Deep learning
Tabular prior-data fit network (TabPFN)
ACAM-NSGA-II
Multi-objective optimization

ABSTRACT

Carbon capture, enhanced oil recovery (EOR)-utilization and storage (CCUS-EOR) is recognized as an effective approach to mitigate greenhouse gas emissions while delivering economic benefits. However, its practical deployment is limited by the absence of advanced deep learning models for petroleum tabular data, the limited adaptability of existing optimization methods, and the lack of comprehensive evaluation for full-cycle CCUS-EOR. Here, we introduce a generalizable framework that integrates mechanism experiments, numerical simulations, and deep learning methods to address these challenges. Three-stage experiments are conducted to clarify microscopic displacement mechanisms and provide key parameters for numerical simulation. Based on field-scale simulations of 20 years of CO_2 water-alternating-gas (WAG) injection followed by 19 years of pure CO_2 storage until 2060, we develop a TabPFN-based meta-learning surrogate model for joint prediction of oil recovery, CO_2 storage, and net present value (NPV), achieving high accuracy (prediction error <2%, $R^2 > 0.97$) compared to baseline models. We further apply an improved multi-objective optimization using the Adaptive Crossover and Adaptive Mutation Non-dominated Sorting Genetic Algorithm II (ACAM-NSGA-II) to obtain optimal Pareto solutions. Compared to baseline cases, the proposed framework significantly enhances CCUS-EOR performance, enhancing oil recovery by 27.05% (from 5.95×10^5 t, 35.17% to 1.05×10^6 t, 62.22%), tripling CO_2 storage capacity (from 1.33×10^6 to 4.45×10^6 t), and improving NPV by 68.0% (from \$344 million to \$578 million). The Pareto front is further divided into three different solution regions, thereby elucidating the underlying physical mechanisms associated with each cluster and providing clear operational insights for target-oriented CO_2-WAG design. This study offers a scalable blueprint framework for large-scale engineering design in petroleum engineering, particularly in tabular prediction and multi-objective optimization contexts.

1. Introduction

In recent years, global warming has become irreversible due to increasing emissions of greenhouse gases, particularly carbon dioxide (CO_2) (Meinshausen et al., 2009; Solomon et al., 2009). Statistics indicate that global CO_2 emissions reached 36.1 Gt in 2022 (Liu et al., 2023). To address this challenge, carbon capture, utilization, and storage (CCUS) has become one of the most promising strategies for mitigating the greenhouse effect (Dou et al., 2023; Liu et al., 2020; Wei et al., 2021). Among various CCUS approaches, CCUS for enhanced oil recovery (CCUS-EOR) has

---

* Corresponding author.
** Corresponding author.
E-mail addresses: yangsl@cup.edu.cn (S.-L. Yang), hongbo.zeng@ualberta.ca (H.-B. Zeng).

Peer review under the responsibility of China University of Petroleum (Beijing).

https://doi.org/10.1016/j.petsci.2026.01.028

been recognized as an economically viable method, as it not only facilitates carbon storage but also significantly enhances oil recovery (Zhang et al., 2019). Since the 1970s, the number of CO_2 miscible flooding projects has steadily increased (Holm, 1982), demonstrating greater economic advantages compared to other enhanced oil recovery (EOR) techniques such as thermal or chemical flooding, even under low oil price conditions (Martin and Taber, 1992). As a result, CO_2 geological storage in oil and gas reservoirs has become more attractive to operators compared to deep saline aquifers or depleted coal seams (Ren et al., 2022). The introduction of China's “dual-carbon” goal in September 2020 further accelerated the development of CCUS-EOR technologies (Song et al., 2023). Field demonstrations in oilfields such as Jilin and Daqing have shown that CCUS-EOR can improve oil recovery by 10%–25% and achieve CO_2 storage efficiency of 60%–70%, with each 2.0–3.0 t injected CO_2 yielding an additional 1.0 t crude oil, thereby offering clear benefits in both incremental oil production and carbon storage (Yuan et al., 2022). Internationally, the United States and Canada lead CCUS-EOR implementation. In the U.S., the annual oil production from CCUS-EOR exceeded 1000×10^4 t in 1994, rose to 1500×10^4 t by 2012, and remained at 1365×10^4 t in 2020 (Yuan et al., 2022). Policy incentives such as Section 45Q tax credits (\$27–60/ton CO_2) (Ren et al., 2022) have substantially promoted CCUS-EOR adoption. Both in China and globally, large-scale CCUS-EOR deployment offers significant potential for enhancing oil production and supporting carbon neutrality goals.

Extensive laboratory and numerical simulation studies have provided valuable mechanism insights into CO_2-oil interactions in CCUS-EOR processes (Kamali et al., 2017; Zhou et al., 2024). Experimental investigations, including oil swelling tests, slim tube tests, and coreflooding experiments, have been widely conducted to evaluate CO_2 solubility effects, minimum miscibility pressure (MMP), and oil displacement efficiency under reservoir conditions (Z. Li et al., 2022). Therefore, reservoirs planned for CCUS-EOR typically require laboratory experiments prior to field implementation (Zhang et al., 2025). Meanwhile, compositional reservoir simulators such as CMG-GEM have played a crucial role in analyzing the water-alternating-gas (WAG) performance (Kamali et al., 2017; H. Li et al., 2022; B. Liu et al., 2023). Numerous studies have revealed that alternating the injection of water and CO_2 in WAG operations effectively stabilizes the displacement front by mitigating gas channeling and suppressing viscous fingering (He et al., 2023, 2024), thereby improving sweep efficiency and overall displacement uniformity (Zhang et al., 2024). However, these high-fidelity experiments and simulations are often time-consuming and computationally expensive, which greatly limits their scalability in large design-space optimization.

In CCUS-EOR operations, oil production, CO_2 storage capacity, and net present value (NPV) are the three primary performance metrics (H. Li et al., 2022; Ren et al., 2022; You et al., 2020a). Accordingly, considerable research has focused on predicting these metrics in field-scale CO_2 flooding projects. To overcome the limitations of conventional simulations, which suffer from high computational costs, limited adaptability, and low efficiency (Gao et al., 2024, 2025; Song et al., 2024), recent studies have increasingly explored machine learning (ML) approaches to develop reliable predictive models (Wang et al., 2024). For example, (Chen and Pawar, 2019) developed multivariate adaptive regression splines (MARS), support vector regression (SVR), and random forest (RF) models to evaluate oil production and CO_2 storage potential in residual oil zones (ROZ). You et al. (2020b) employed simulation data generated to train an artificial neural network (ANN) for forecasting cumulative oil production, CO_2 storage amount, and NPV under various CO_2-WAG injection scenarios. While these studies demonstrate the potential of ML, most have relied on conventional ML algorithms with inherent limitations. Traditional ML models often lack generalization capability and scalability when applied to small sample datasets in energy and environmental engineering (Chen et al., 2022b). Although deep learning has shown superior capacity to capture complex data patterns (LeCun et al., 2015), its application to tabular data in CCUS-EOR prediction remains limited. Existing deep learning models for tabular data (Shen et al., 2023b) have yet to surpass tree-based models, such as eXtreme Gradient Boosting (XGBoost), in terms of prediction accuracy. Therefore, there is a pressing need for deep learning models that can simultaneously offer high accuracy, scalability, and robustness in predicting CO_2-EOR and storage performance. In addition, from a feature selection perspective, many existing studies rely on only a limited subset of operational parameters for predicting and optimizing CCUS-EOR performance. Most models include injection- and production-related features such as gas and water injection rates, injection time, and bottom-hole pressure, which are widely recognized as key factors influencing oil recovery and CO_2 storage outcomes (Chen and Pawar, 2019; Rui et al., 2025; You et al., 2020a). However, these studies often fail to adopt a full-cycle CCUS-EOR perspective, and thus overlook operational parameters critical to other lifecycle phases. For instance, long-term CO_2 injection rates during the storage phase are rarely considered, despite their strong influence on cumulative storage performance (Rui et al., 2025). Similarly, well-level control variables such as gas-oil ratio (GOR) shutdown limits during the EOR phase are often neglected, despite their proven importance for mitigating gas breakthrough and enhancing economic returns (Pereira et al., 2022). These omissions restrict the models' ability to fully capture system dynamics across all stages of CCUS-EOR operations. Therefore, there is a pressing need for deep learning models that can achieve both high predictive accuracy and comprehensive feature inclusion, enabling reliable performance forecasting for oil recovery, CO_2 storage, and economic evaluation across the entire CCUS-EOR lifecycle.

Moreover, machine learning models in CCUS-EOR are often coupled with multi-objective optimization techniques to efficiently explore optimal operational strategies. In practice, petroleum engineers typically seek to balance multiple objectives simultaneously, such as maximizing oil recovery, CO_2 storage, and economic returns, rather than optimizing a single target. Various multi-objective optimization algorithms have been employed to address this challenge, including multi-objective particle swarm optimization (MOPSO) (Christie et al., 2013; Zhuang et al., 2024), multi-objective genetic algorithms (MOGA) (Han et al., 2010), and non-dominated sorting genetic algorithm II (NSGA-II) (Safarzadeh and Motahhari, 2014). For instance, You et al. (2020b) proposed a robust optimization framework combining multilayer neural networks with MOPSO, successfully optimizing oil production, CO_2 storage amount, and NPV in the Farnsworth CO_2-WAG project in Texas. Similarly (Safarzadeh and Motahhari, 2014) used NSGA-II to simultaneously optimize CO_2 storage and oil production. However, existing multi-objective optimization methods exhibit limited adaptability. Specifically, conventional crossover operators often lack sufficient global exploration capability, while polynomial mutation operators introduce excessive randomness, both of which restrict the overall optimization performance. Therefore, there is an urgent need for novel, more adaptive multi-objective optimization algorithms that can more effectively explore the solution space and enhance the optimization of CO_2-EOR and storage performance.

In addition, the synergistic optimization of CO_2-EOR and geological storage requires a multi-scale, cross-disciplinary integration framework capable of supporting full-lifecycle CCUS-EOR performance prediction and decision-making (Rui et al., 2025).

However, most existing studies focus on only one or two dimensions, such as pore-scale or core-scale experiments (Yang et al., 2024), reservoir-scale numerical simulation (Chen and Reynolds, 2016), or machine learning modeling (Shen et al., 2023a). A few studies attempt to couple experimental and numerical approaches (Kamali et al., 2017; Li et al., 2022b), yet these efforts still fall short of integrating all three components into a unified, mechanism-guided computational framework. While each method provides valuable insights, the lack of integration across experimental observations, physical modeling, and data-driven approaches has resulted in the fragmented understanding of the CO_2-oil interaction mechanisms and limited the applicability and scalability of predictive models and optimization workflows in real-world scenarios. To date, no research has clearly demonstrated how to systematically combine pore-scale experimental evidence, reservoir-scale simulations, and machine learning models into a coherent and generalizable framework for CCUS-EOR planning and operation. This methodological gap is especially critical under the pressing carbon neutrality agenda, where high-fidelity mechanistic representation and computational efficiency must go hand-in-hand. Bridging this gap is essential to unlock the full potential of CO_2-WAG strategies, enabling the simultaneous achievement of enhanced oil recovery and long-term carbon sequestration in large-scale, field-deployable CCUS-EOR applications.

Based on the above review, this study identifies three critical research gaps that remain unresolved: (1) **Insufficient feature comprehensiveness and limited representational capability of existing ML models.** Conventional ML algorithms (e.g., SVR, RF, and XGBoost) are often constrained by shallow architectures and weak generalization, making them incapable of capturing the nonlinear and coupled effects among CO_2 injection, production control, and reservoir parameters. Consequently, most existing models only include a subset of operational parameters, overlooking critical full-cycle features such as well-level GOR shutdown limits during the EOR phase and CO_2 injection rates during the storage phase. In contrast, deep learning provides strong representational capability and generalization, enabling comprehensive characterization of operational dependencies across the CCUS-EOR lifecycle. However, its potential for accurate performance prediction (e.g., oil recovery, CO_2 storage, and NPV) remains largely unexplored. (2) **Limited adaptability and robustness of current multi-objective optimization algorithms.** Existing algorithms such as MOPSO, MOGA, and NSGA-II exhibit weak global exploration during crossover and excessive randomness in mutation, often leading to premature convergence and reduced Pareto diversity. These shortcomings hinder their ability to identify high-quality, balanced solutions across competing objectives such as oil recovery, CO_2 storage, and economic return. Therefore, adaptive strategies should be further investigated to enhance exploration capability and solution diversity. (3) **Lack of an integrated framework for full-cycle CCUS-EOR evaluation and optimization.** Most studies isolate different research dimensions, including mechanism experiments, reservoir simulations, and data-driven modeling, rather than integrating them into a unified workflow. This fragmentation limits the understanding of dynamic trade-offs and physical mechanisms that govern system behavior, leading to predictions and optimization results that deviate from field realities and carbon neutrality objectives. Therefore, developing an integrated framework that enables full-cycle evaluation and decision-making should be further investigated to achieve physically consistent and practically feasible CCUS-EOR optimization.

To bridge these research gaps, this study proposes a novel, generalizable framework that integrates mechanism experiments, numerical simulations, and deep learning methods. This unified framework is designed to predict and optimize both CO_2 storage and economic return in real-world CCUS-EOR projects under carbon neutrality targets. A schematic overview illustrating the integrated workflow is shown in Fig. 1. Taking the S oilfield as a case study, we conduct a three-stage experimental approach comprising oil swelling tests, slim tube tests, and high-temperature high-pressure long-core flooding experiments. These experiments provide critical high-fidelity inputs, including accurate crude oil properties and MMP measurements, which are incorporated into dynamic reservoir simulations. Building on these detailed mechanistic insights, we perform Monte Carlo simulations using CMG-GEM (Computer Modeling Group Ltd., Calgary, AB, Canada) to explore 1147 field-scale and full-cycle CO_2-WAG scenarios under varying operational parameters. To enhance predictive accuracy and adaptability, we develop a state-of-the-art meta-learning surrogate model based on the Tabular Prior-data Fit Network (TabPFN) and integrate it with an Adaptive Crossover and Adaptive Mutation Non-dominated Sorting Genetic Algorithm II (ACAM-NSGA-II). This combined approach enables rapid, high-precision joint prediction and optimization of cumulative oil production, CO_2 storage, and net present value (NPV). Beyond conventional optimization, we introduce an innovative application of the K-means clustering algorithm to systematically partition the Pareto front into distinct solution regions, each representing

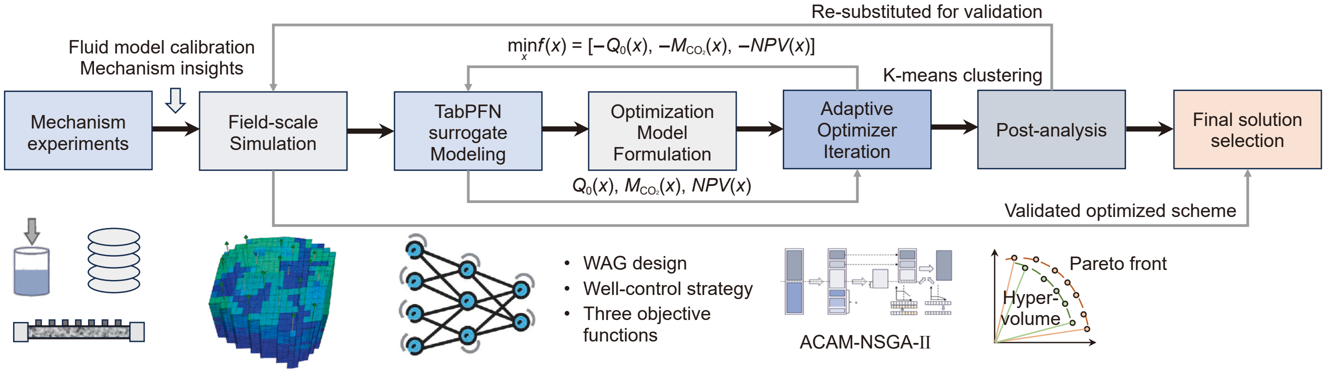

Fig. 1. Schematic diagram of the integrated framework combining mechanism experiments, numerical simulation, TabPFN surrogate modeling, and ACAM-NSGA-II optimization, followed by Pareto clustering and post-validation.

different operational trade-offs. This partitioning clarifies the underlying mechanisms governing system behavior under varied injection strategies and provides actionable insights for decision-making and large-scale deployment of CCUS-EOR technologies under carbon neutrality constraints.

2. Background and methods

2.1. Experimental setup and methods

In this section, we will describe a three-stage experimental system (Fig. 2) consisting of oil swelling tests, slim tube tests, and coreflooding experiments.

The Ruska PVT-2370 high-temperature and high-pressure physical property analyzer was used to prepare the formation crude oil and conduct oil swelling tests (Fig. 2(a)). Crude oil samples were collected from the S block of the Tuha Oilfield, and their composition was analyzed using a high-temperature gas chromatograph. The formation crude oil was prepared following the national standard GB/T 26981-2020, “Analysis Method of Physical Properties of Oil and Gas Reservoir Fluids”. Table 1 summarizes the compositions of the dissolved gas, dead oil, and live oil. Oil swelling tests were conducted using the prepared crude oil samples. The detailed experimental procedure is as follows: (1) The thermostatic chamber was set to the reservoir temperature of 82.6 °C and preheated for at least 4 h to ensure uniform thermal distribution. (2) The PC cell, FPC cell, and viscometer loop were cleaned with petroleum ether, followed by three cycles of CO_2 purging and displacement to eliminate residual air from system. (3) Crude oil was injected from the bottom of the PC cell until it occupied 1/2 to 1/3 of the cell volume, after which the injection valve was closed. The molar amount of crude oil was determined based on its mass and molar mass to facilitate calculation of the required CO_2 injection volume. (4) A predetermined molar fraction of CO_2 was injected from the top of the FPC cell, and the CO_2 injection valve was then closed. The injected CO_2 was fully compressed into the PC cell to mix with the crude oil, and the PC-FPC intermediate valve was closed. After thermal stabilization for at least 4 h, the system pressure was gradually increased while the mixture was continuously stirred using an electromagnetic stirrer to ensure complete dissolution of CO_2 into the crude oil, forming a CO_2-oil system. The saturation pressure and swelling factor were recorded when the final gas bubble disappeared. (5) The PC-FPC intermediate valve was reopened, allowing a portion of the saturated oil to flow into the FPC cell, where its viscosity is measured using a high-temperature and high-pressure viscometer. The measured saturated oil was then reinjected into the PC cell, and oil viscosity measurements were repeated until two consecutive readings were consistent to ensure experimental repeatability. (6) The experiment was repeated eight times, adjusting the CO_2 injection molar fraction from 0% to 70% in increments of 10%.

Table 1
Compositions of dissolved gas, dead oil, and live oil.

Component	Dissolved gas, mol%	Dead oil, mol%	Live oil, mol%
CO_2	0.034	0	0.02
N_2	2.103	0	1.32
CH_4	65.72	0	41.57
C_2H_6	11.804	0	7.46
C_3H_8	9.805	1.38	6.76
iC_4	4.137	3.02	3.72
nC_4	3.439	2.61	3.13
iC_5	1.353	4.64	2.55
nC_5	0.827	2.54	1.45
C_6	0.474	6.41	2.65
C_{7+}	0.214	79.4	29.3

The slim tube tests were conducted to determine the MMP of the CO_2-oil system, which is a critical parameter for evaluating CO_2

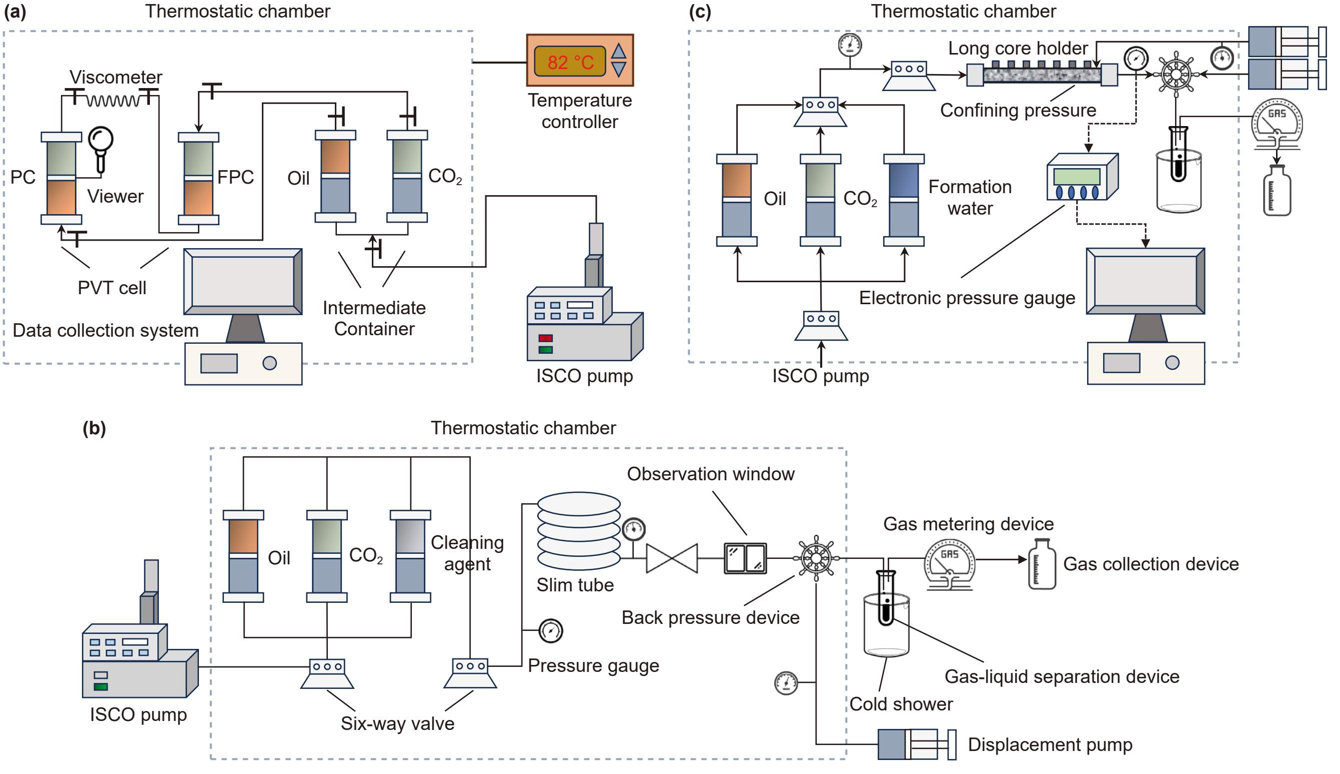

Fig. 2. Schematic diagram of the three-stage experimental system. Equipment schematics of **(a)** the oil swelling tests, **(b)** the slim tube tests, and **(c)** the coreflooding experiments.

flooding potential. The experiments followed the petroleum industry standard SY/T 6573-2016 ("Minimum Miscible Pressure Experimental Determination Method — Slim Tube Method"), with the experimental setup shown in Fig. 2(b). The slim tube, measuring 0.46 cm in diameter and 12.51 m in length, was packed with quartz sand (porosity: 36.88%, permeability: 5.30 mD). The experimental procedure was as follows: (1) The pipeline was flushed with petroleum ether until the inlet and outlet compositions stabilized, followed by drying with high-pressure nitrogen and subsequent heating at 82.6 °C for 6 h. The slim tube was then evacuated for 4 h. (2) The slim tube was saturated with crude oil at 82.6 °C and the designated pressure**.** The back pressure was set to the target experimental pressure. The intermediate container valve and the tube inlet valve were opened. Two pore volumes (PV) of crude oil were injected at 1 mL/min, and outlet fluid compositions were measured every 0.1 PV. Saturation was deemed complete when the outlet composition matched that of the formation oil. (3) CO_2 was injected using an ISCO pump at a pressure 0–0.5 MPa above the experimental pressure**,** with a constant injection rate of 0.1 mL/min. If the displacement pressure drop exceeded 0.5 MPa, the injection rate was reduced accordingly. The flooding process continued until 1.2 PV CO_2 was injected or until oil production ceased. (4) The volumes of produced oil and gas at various injected PVs were recorded, along with injection pressure and backpressure values, to calculate the oil recovery factor. The experiment was repeated six times under varying experimental pressures (12.5, 16.7, 19.3, 22.4, 24.6, and 28.4 MPa).

Additionally, coreflooding experiments were conducted to investigate oil recovery and carbon storage potential at the microscopic scale. The core samples were obtained from natural reservoir rocks in the S oilfield. Ten core plugs, with a cumulative length of 79.36 cm, were selected. The basic parameters of the core samples are listed in Table 2, and the experimental setup is shown in Fig. 2(c). The experimental steps were as follows: (1) The core samples were cleaned with petroleum ether, dried using high-pressure nitrogen, and then vacuumed for 36 h. (2) After saturating the cores with formation water, formation oil was injected at 82.6 °C and 28.8 MPa to displace the formation water, establishing irreducible water saturation. (3) Water flooding was conducted at an injection rate of 0.1 mL/min until the water cut reached 90%. (4) CO_2-WAG injection was then conducted, with each WAG cycle consisting of a 0.2 PV slug size and a gas-to-water ratio of 1:1, meaning 0.1 PV CO_2 was injected followed by 0.1 PV water, both at 0.1 mL/min. Produced gas was collected using a gas sampling system, while injection pressure, backpressure, pump readings, and oil and gas production volumes were recorded. The gas breakthrough time is identified as the moment when gas first appears at the outlet, typically indicated by a sharp increase in the gas-oil ratio (GOR). (5) For continuous CO_2 flooding, the cores were cleaned after completing a WAG test, and Steps (1) to (3) were repeated. Following water flooding, continuous CO_2 injection was carried out at 0.1 mL/min without water alternation.

Table 2
Properties of core samples.

Laboratory ID	Diameter, cm	Length, cm	Permeability, mD	Porosity, %
1	2.468	7.678	13.580	13.42
2	2.466	7.323	14.988	11.88
3	2.464	8.375	15.794	11.87
4	2.466	8.466	15.889	11.57
5	2.466	7.558	17.042	11.93
6	2.467	8.366	17.698	11.58
7	2.466	8.305	22.204	12.19
8	2.466	7.965	25.076	12.11
9	2.468	7.427	33.015	12.10
10	2.468	7.898	45.034	13.24
Average	2.467	79.361	19.237	12.18

2.2. *Numerical simulation of CO_2-WAG injection*

2.2.1. *Fluid model calibration*

Before conducting full-field numerical simulations, the fluid model was rigorously calibrated using experimental measurements to ensure consistency between laboratory-scale observations and reservoir-scale predictions. Specifically, key fluid properties derived from oil swelling tests and slim tube tests, including the swelling factor, viscosity variation, and MMP, were used to refine the PVT and EOS modules in the CMG-GEM simulator. These parameters were critical for accurately capturing the complex phase behavior and miscibility transitions of the CO_2-oil system under reservoir conditions. By anchoring the fluid model to experimental data, this calibration step provided a robust physical foundation for subsequent simulation and optimization work, enhancing the reliability and interpretability of both numerical predictions and machine learning-guided analyses.

2.2.2. *Reservoir description and simulation setup*

The study area is a typical low-permeability oilfield located in the Tuha Basin of Xinjiang, with a burial depth ranging from 2158 to 2793 m and geological reserves of 35.23 million tons. The average permeability is 6.15 mD, porosity is 12.5%, and average water saturation is 0.58. Due to the large scale of the full-field model (716,220 grid blocks), a representative submodel was extracted to reduce computational cost, as shown in Fig. 3. The submodel preserves the key physical features of the original system (e.g., average permeability, porosity, and water saturation) and effectively represents the reservoir's overall characteristics (Table S1 in Supplementary A). It consists of four injection wells and fifteen production wells, with a geological reserve of 1.69 million tons and an average well spacing of 417 m. The grid is discretized into 20 × 18 × 25 blocks, with a thickness of 444 m and a depth range of 2203–2647 m. The top boundary was set as constant pressure to represent aquifer connection, while the others were defined as no-flow boundaries. Key parameters are summarized in Table S2. Based on over 30 years of field production data under waterflooding development since 1990, a numerical simulation model was constructed using CMG-GEM (2022 version). The model has been thoroughly history-matched and verified by field engineers, as shown in Fig. S1 (Supplementary A) through the consistent matches of cumulative oil production, average reservoir pressure, and water production rates. It incorporates a wide range of geological and operational parameters. Further details, such as the oil-water relative permeability relationships, are provided in our previous studies (Shen et al., 2024; Xiao et al., 2024).

A total of 1147 parameterized Monte Carlo simulations were conducted, including 20 years of CO_2-WAG injection followed by 19 years of continuous storage (until 2060). The key simulation parameters and optimization ranges are summarized in Table 3. The optimization focuses on two aspects: (1) WAG design: Gas and water injection times and rates were independently optimized rather than through an overall slug size, as they directly affect reservoir pressure stability, displacement front advancement, and

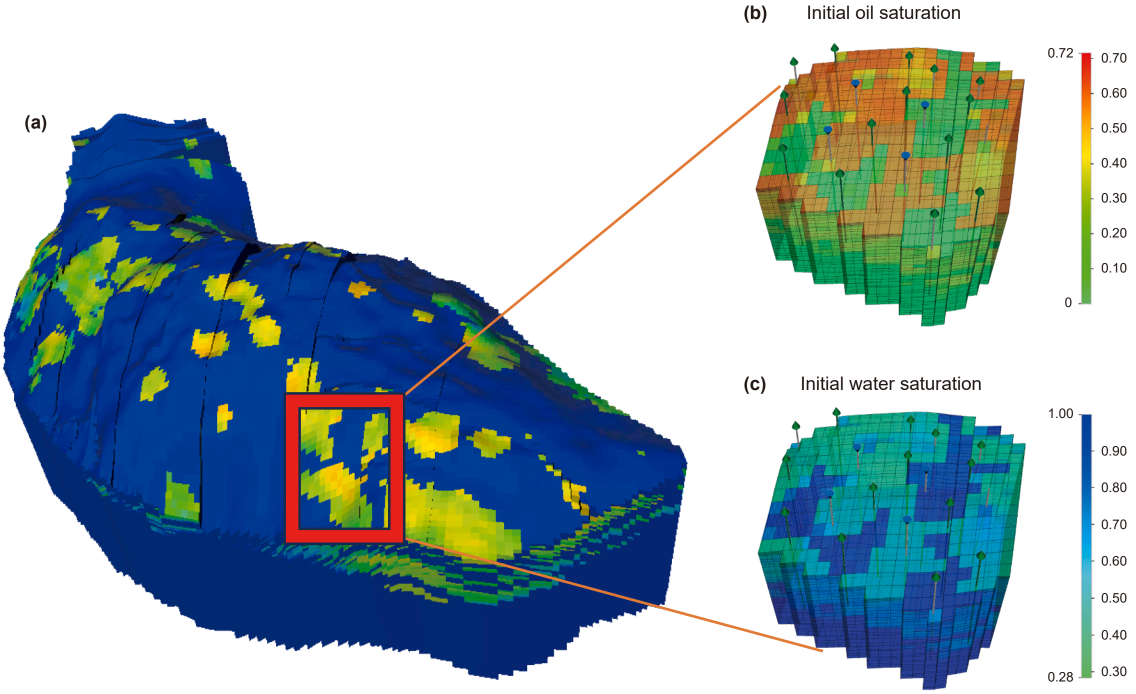

Fig. 3. Visualization of field-scale reservoir model. **(a)** Full-field reservoir model, **(b)** initial oil saturation, and **(c)** initial gas saturation of the extracted submodel containing 4 injection wells (blue) and 15 production wells (green).

Table 3
Parameter ranges of Monte Carlo simulation experiments (within one WAG cycle).

Category	Parameters	Min	Max
WAG design	Gas injection rate in the EOR stage, m^3/d	69,841.70	468,752.31
	Water injection rate, m^3/d	12.18	887.86
	Gas injection time, d	78.87	412.95
	Water injection time, d	78.77	397.88
	Gas injection rate in the CO_2 storage stage, m^3/d	10,008.88	59,340.12
Well-control conditions	Bottom hole pressure of injection wells, MPa	33.01	58.01
	Bottom hole pressure of production wells, MPa	19.28	36.56
	Surface liquid production rate of production wells, m^3/d	19.34	169.11
	Production well shut-in gas-oil ratio, m^3/m^3	1426.97	5526.33
	Global shut-in gas-oil ratio, m^3/m^3	637.77	4328.07

sweep efficiency, thereby influencing gas channeling, oil recovery, and CO_2 storage. Historical data (Fig. S2) show that the maximum single-well water injection rate during waterflooding was below 150 m^3/d, with six injectors operating in total, and the overall field injection rate did not exceed 900 m^3/d; thus, this value was used as the upper limit in the simulations for four WAG injectors. (2) Well-control strategy: A combined control scheme was applied with both bottom-hole pressure (BHP) and surface total liquid rate (STL) constraints, giving priority to BHP. Additional well- and field-level GOR limits governed well shut-in operations. The maximum BHP was set to 58 MPa (below the 60 MPa fracture pressure, providing a safety margin of 0%–5%), and the minimum near the MMP (20.87 MPa) to ensure near-miscible flooding. This strategy balanced injection safety, operational flexibility between rate- and pressure-control modes, and prevention of gas breakthrough.

2.3. Target variable modeling

2.3.1. Cumulative oil production and oil recovery

The cumulative oil production and oil recovery are calculated using the following equations (Azzolina et al., 2015):

$$\text{Cumulative oil production} = \sum_{t=1}^{T} q_{\text{oil},t} \cdot \Delta t \tag{1}$$

$$\text{Oil Recovery} = \frac{\text{Cumulative oil production}}{\text{OOIP}} \times 100\% \tag{2}$$

where $q_{\text{oil},t}$ denotes the oil production rate at the time step,Δt represents the duration of the time step, T represents the total number of time steps in the EOR production period. OOIP denotes the original oil in place.

2.3.2. CO_2 storage

To accurately evaluate CO_2 storage performance, we adopt the following formula to calculate the CO_2 storage amount (Melzer, 2012):

$$CO_2\ \text{storage} = \text{Total}\ CO_2\ \text{injected} - CO_2\ \text{produced} - CO_2\ \text{losses} \tag{3}$$

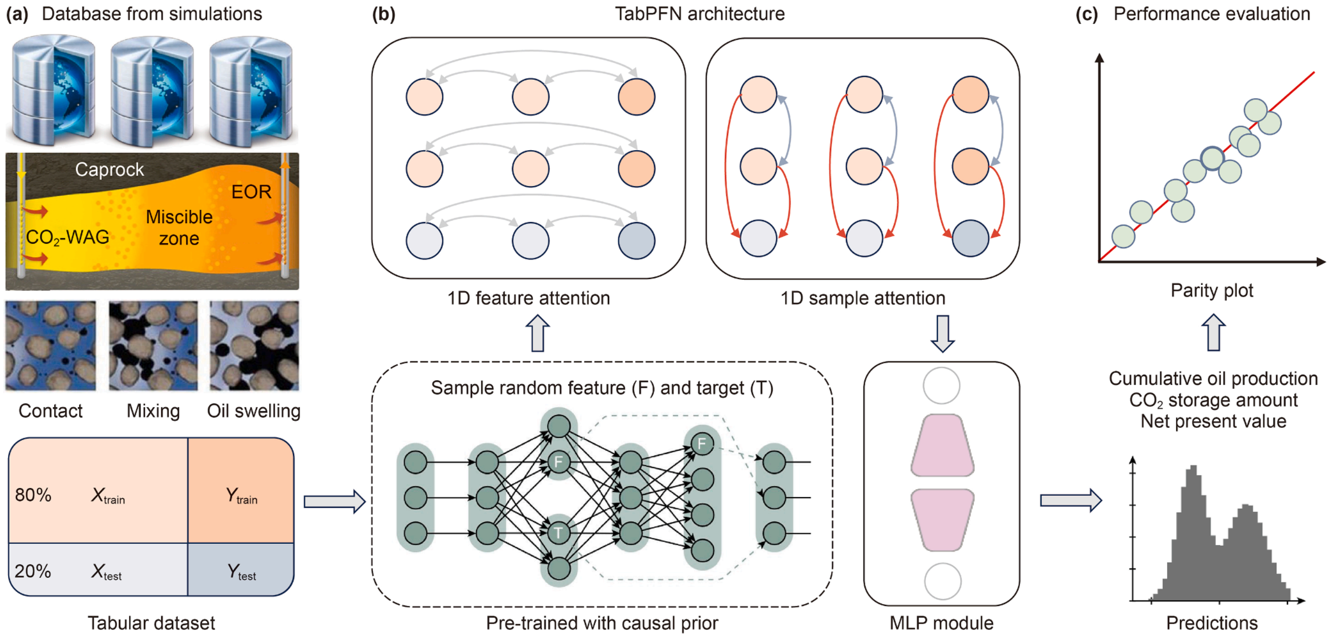

Fig. 4. Overview of TabPFN for CO_2-WAG prediction. **(a)** CO_2-WAG simulation-generated tabular dataset, **(b)** TabPFN architecture incorporates causal priors, two-way attention, and Bayesian inference, **(c)** prediction and performance evaluation, including uncertainty quantification and parity analysis.

where total CO_2 injected refers to the combined CO_2 injection during both the EOR and storage stages. CO_2 produced represents the cumulative amount of CO_2 produced during the EOR phase. CO_2 losses include losses due to surface operations (e.g., venting or blowdowns) and potential subsurface leakage. In this study, CO_2 losses are assumed to be negligible (i.e., set to zero) given their typically low contribution.

2.3.3. Net present value (NPV)

Considering key economic factors such as oil revenue, CO_2 purchase and operational costs, and carbon tax credits (Ren et al., 2022; You et al., 2020b), the net present value (NPV) formulas used in this study are detailed as follows:

$$\mathrm{NPV}=\sum_{n=1}^{N}\left[\frac{\mathrm{Oil}_{\mathrm{revenue}_n}}{(1+p)^n}-\frac{\mathrm{Operation}_{\mathrm{cost}_n}}{(1+p)^n}+\frac{\mathrm{Carbon}_{\mathrm{price}_n}}{(1+p)^n}\right] \tag{4}$$

$$\mathrm{NPV}=\sum_{n=1}^{N}\left[\frac{Q_{\mathrm{opn}}\times\mathrm{Oil}_{\mathrm{price}}}{(1+p)^n}-\frac{Q_{\mathrm{win}}\times\mathrm{Water}_{\mathrm{cost}}+Q_{\mathrm{gin}}\times\mathrm{Gas}_{\mathrm{pur}}+Q_{\mathrm{gpn}}\times\mathrm{Gas}_{\mathrm{rec}}}{(1+p)^n}+\frac{\left(Q_{\mathrm{gin}}-Q_{\mathrm{gpn}}\right)\times\mathrm{Storage}_{\mathrm{cost}}}{(1+p)^n}\right] \tag{5}$$

where $\mathrm{Oil}_{\mathrm{revenue}_n}$ is the revenue from oil production in year n (\$), $\mathrm{Operation}_{\mathrm{cost}_n}$ is the operating cost, and $\mathrm{Carbon}_{\mathrm{price}_n}$ is the incentive for CO_2 storage. p is the discount rate. Q_{opn} is the oil production (ton), and $\mathrm{Oil}_{\mathrm{price}}$ is the oil price (\$/ton). Q_{win} and Q_{gin} are cumulative water and CO_2 injection volumes, with costs $\mathrm{Water}_{\mathrm{cost}}$ and $\mathrm{Gas}_{\mathrm{pur}}$. Q_{gpn} is the CO_2 production (ton), $\mathrm{Gas}_{\mathrm{rec}}$ is the recycling cost, and $\mathrm{Storage}_{\mathrm{cost}}$ is the carbon tax credit (\$/ton).

We consider a \$35/ton carbon tax credit based on projections through 2060 (Ren et al., 2022). To simplify the analysis, we assume a zero discount rate, eliminating time-value effects and focusing on optimization results. Other economic parameters follow (Ren et al., 2022): $\mathrm{Oil}_{\mathrm{price}}$ = \$60/STB, $\mathrm{Gas}_{\mathrm{pur}}$ = \$25.2/ton, $\mathrm{Gas}_{\mathrm{rec}}$ = \$0.6/MSCF, and $\mathrm{Water}_{\mathrm{cost}}$ = \$0.85/STB.

2.4. Deep learning methods for predicting CO_2-EOR and storage performance

The Tabular Prior-data Fitted Network (TabPFN) (Hollmann et al., 2025) is a pre-trained deep learning model specifically designed for predictive tasks on small to medium-sized tabular datasets (typically with thousands of samples) using in-context learning (ICL) (Dong et al., 2024). Its architecture is illustrated in Fig. 4. TabPFN is a variant of the original Transformer encoder (Vaswani et al., 2017) combined with the Prior-Data Fitted Network (PFN) framework (Müller et al., 2024), integrating causal prior pretraining with a Transformer-based neural architecture for tabular data. Specifically, TabPFN is pre-trained on synthetic tabular datasets generated via structural causal models (SCMs), which encode diverse causal relationships serving as prior knowledge. This pretraining process enables TabPFN to approximate the posterior predictive distribution (PPD) (Nagler, 2023), effectively equipping the model with meta-learning capabilities (Hospedales et al., 2022) and superior out-of-distribution (OOD) generalization compared to conventional machine learning models. A key architectural innovation in PFN is the two-way attention mechanism, which operates both row-wise (attending to other features within a sample) and column-wise (attending to the same feature across all samples). This design ensures invariance to sample and feature ordering while enhancing training efficiency. During inference, TabPFN leverages ICL to perform label estimation and Bayesian prediction on real-world datasets. Originally popularized in large language models, ICL has demonstrated efficacy in enabling Transformers to learn a wide range of underlying algorithms, from simple to complex tasks.

In this CO_2-WAG prediction task, the end-to-end workflow of TabPFN is as follows: the full-cycle numerical simulation produces a total of 1147 samples, which are split into an 80:20 training-to-test ratio. All data are directly fed into the pre-trained TabPFN, which has been trained on synthetic causal datasets. During inference, the 229 testing samples are concatenated with the training set using ICL. A single forward pass is performed, wherein input features are processed via a 1D feature and sample attention encoder to capture data dependencies, followed by an multilayer perceptron (MLP) module that predicts target labels along with Bayesian uncertainty estimates. Model performance and uncertainty calibration are evaluated through parity plots and reliability diagrams.

2.5. Multi-objective optimization for enhancing CO_2-EOR and storage performance using the ACAM-NSGA-II algorithm

The Adaptive Crossover and Adaptive Mutation Non-dominated Sorting Genetic Algorithm II (ACAM-NSGA-II) is an improved evolutionary algorithm tailored for multi-objective optimization problems. Building upon the classical NSGA-II framework (Deb et al., 2002), ACAM-NSGA-II integrates dynamic adjustment mechanisms for both crossover and mutation operations to enhance global exploration and mitigate excessive randomness. Fig. 5 outlines the overall procedure of ACAM-NSGA-II, which includes population initialization, adaptive genetic operations, non-dominated sorting, crowding distance calculation, environmental selection, and iterative evolution. The algorithm proceeds as follows: (1) Population initialization: An initial parent population P_t of size N is randomly generated. Offspring population Q_t is produced using adaptive genetic operators, specifically incorporating adaptive crossover and mutation strategies. The parent and offspring populations are merged to form R_t of size $2N$. (2) Non-dominated sorting and crowding distance calculation: Fast non-dominated sorting is applied to R_t, dividing individuals into multiple non-dominated fronts F_1, F_2, … …, F_k, where F_1 represents the best individuals in the current population, followed by F_2, F_3, and so on. Within each front, the crowding distance is then computed to assess solution diversity in the objective space. (3) Environmental selection (forming the new parent population P_{t+1}): Suitable individuals are selected based on the dominance ranking and crowding distance to construct the new parent population P_{t+1} until reaching the population size N. If a particular front exceeds the remaining allocation, individuals with larger crowding distances are preferentially retained to maintain population diversity. (4) Iterative offspring generation: Finally, the adaptive crossover and mutation strategies are applied to generate the new offspring population Q_{t+1}. The new population P_{t+1} is then merged with Q_{t+1} to form R_t, and the process repeats until the optimization termination condition (e.g., maximum number of generations) is met. Throughout the iterations, the population evolves continuously, ultimately converging to the Pareto-optimal front.

The adaptive mechanisms embedded in ACAM-NSGA-II significantly improve convergence and population diversity, outperforming conventional fixed-parameter evolutionary algorithms. In contrast, fixed crossover and mutation rates restrict global exploration and introduce excessive randomness, ultimately degrading overall optimization performance. The pseudocode of ACAM-NSGA-II, along with the detailed formulations of its adaptive operators, is presented in Supplementary A. Specifically, the algorithm dynamically adjusts the crossover probability P_c and mutation probability P_m based on fitness values (Abdelhafez et al., 2019; Peng et al., 2021), while the crossover distribution index η_c and mutation distribution index η_m are adaptively tuned according to the generation count (Yi et al., 2018). The mathematical formulations of P_c, P_m, η_c, and η_m are detailed as follows:

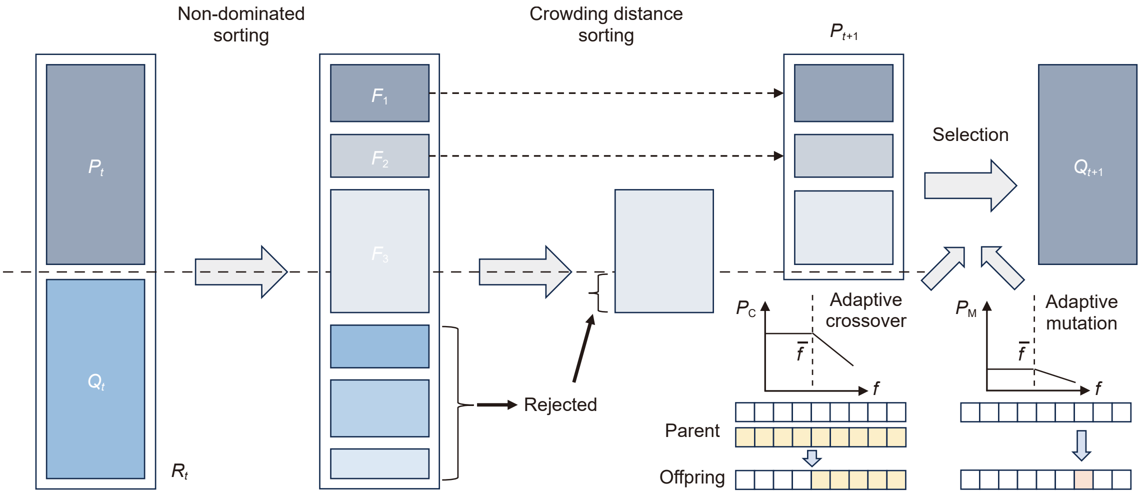

Fig. 5. Schematic representation of the ACAM-NSGA-II optimization process. It involves non-dominated sorting, crowding distance sorting, and adaptive genetic operations (selection, adaptive crossover, and adaptive mutation) to evolve populations and generate high-quality Pareto fronts. The crossover and mutation probabilities (P_c, P_m) are dynamically adjusted according to individual fitness relative to the population average. Specifically, P_c controls the probability that two selected parents undergo crossover to exchange genetic segments, while P_m determines the probability of mutating each gene in the offspring based on its fitness distance from the optimal solutions.

$$P_c = \begin{cases} k_1 \times \sum \left(\dfrac{f_{\max} - f_i}{f_{\max} - f_{\min} + \varepsilon} \right), \text{if} \quad f_i \geq \bar{f} \\ k_2, \qquad\qquad\qquad\qquad\qquad \text{otherwise} \end{cases} \tag{6}$$

$$P_m = \begin{cases} k_3 \times \sum \left(\dfrac{f_{\max} - f_i}{f_{\max} - f_{\min} + \varepsilon} \right) \Big/ D, \text{if} \quad f_i \geq \bar{f} \\ k_4/D, \qquad\qquad\qquad\qquad\qquad\qquad \text{otherwise} \end{cases} \tag{7}$$

$$\eta_c = \eta_{\max} - (\eta_{\max} - \eta_{\min}) \times \frac{G}{G_{\max}} \tag{8}$$

$$\eta_m = \eta_{\min} + (\eta_{\max} - \eta_{\min}) \times \frac{G-1}{G_{\max}-1} \tag{9}$$

where f_i denotes the i-objective fitness values of the selected individuals. . $f_{\max}$, $f_{\min}$, and $\bar{f}$ represent the maximum, minimum, and average fitness values of the current population, respectively. The coefficients k_1 and k_2 control the upper and lower bounds of crossover probability. A small constant ε is introduced to avoid division by zero. D denotes the problem dimensionality. G and $G_{\max}$ correspond to the current and maximum generation numbers. $\eta_{\min}$ and $\eta_{\max}$ represent the minimum and maximum distribution indices.

In the proposed adaptive strategy, individuals with superior fitness are allocated lower crossover and mutation probabilities, whereas those with inferior fitness receive higher probabilities. The individuals whose fitness values fall below the population average receive relatively low crossover probabilities, whereas superior individuals are assigned significantly higher crossover rates (with k_1 set much larger than k_2). This strategy effectively suppresses the propagation of inferior solutions while enhancing diversity among promising candidates. For mutation, k_3 and k_4 are selected to be similar in magnitude, ensuring that high-quality individuals undergo minimal perturbation to preserve advantageous traits and prevent premature convergence, while inferior individuals are subjected to more aggressive mutation to explore alternative solutions. Furthermore, the crossover distribution index η_c decreases progressively over iterations, encouraging local exploitation in early generations and promoting broader exploration in later stages to avoid local optima stagnation. In contrast, the mutation distribution index η_m is initially set to a low value to facilitate broad exploration and gradually increases throughout the generations, narrowing perturbation ranges to facilitate fine-tuning and convergence. Additionally, as crossover operations typically start from generation zero while mutation iterations may begin at one, careful boundary control of η_c and η_m is implemented to maintain consistency. Lastly, since crossover acts on pairs of individuals, while mutation perturbs decision variables independently, mutation probabilities are normalized by the problem dimensionality to ensure balanced mutation intensity across variables.

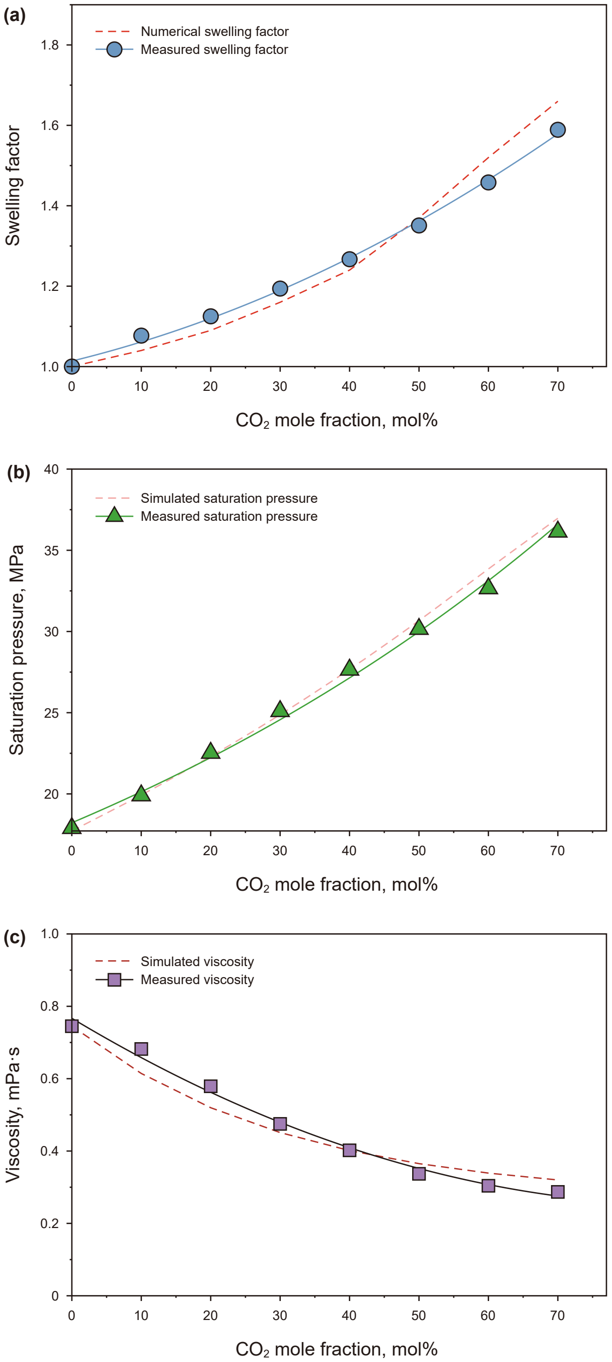

Fig. 6. Results of oil swelling tests: variation of **(a)** swelling factor, **(b)** saturation pressure, and **(c)** oil viscosity at varying CO_2 mole fraction. Solid lines represent the fitted curves from experimental data, while dashed lines correspond to numerical simulation results.

3. Results and discussion

3.1. Experimental results

3.1.1. Oil swelling tests

The high-temperature and high-pressure physical properties of various CO_2-crude oil systems were evaluated through oil swelling tests, focusing on the oil swelling factor, saturation pressure, and oil viscosity. The results reveal excellent CO_2 solubility in the target reservoir crude oil, substantially modifying its rheological characteristics. As the CO_2 molar fraction increases, the swelling factor rises to 1.589 at 70% molar fraction, an overall increase of 58.9% (Fig. 6(a)), demonstrating the effectiveness of CO_2-induced oil expansion in enhancing displacement efficiency. Beyond 30% molar CO_2 injection, the oil swelling factor increases more sharply, indicating improved solubility under higher pressure conditions. At 70% mol CO_2 injection, the saturation pressure rises to 36.14 MPa (Fig. 6(b)), surpassing the original reservoir pressure (28.8 MPa) and approaching the current reservoir pressure (36.56 MPa) after water flooding. This suggests that CO_2-induced oil expansion benefits post-waterflooding oil recovery. Under these conditions, miscibility between CO_2 and crude oil is achieved (MMP: 20.87 MPa), further improving displacement efficiency. Additionally, CO_2 injection significantly lowers crude oil viscosity, which declines to 0.287 mPa s at 70% mol injection (Fig. 6(c)), representing a 61.5% reduction that enhances oil mobility and promotes higher recovery rates. However, the high gas-to-oil viscosity ratio may increase the risk of unstable gas breakthrough, underscoring the importance of CO_2-WAG injection to improve sweep efficiency and ensure stable oil recovery.

3.1.2. *Slim tube tests for minimum miscibility pressure of the CO_2-oil system*

The slim tube experiment was conducted to determine the MMP between CO_2 and crude oil. At experimental pressures of 12.5 and 16.7 MPa, the system exhibited non-miscible displacement behavior, with relatively low oil recovery factors of 46.37% and 66.69% (Fig. 7), respectively. At 19.3 MPa, the system displayed near-miscible displacement characteristics, achieving an 82.96% oil recovery, though still below the 90% miscibility threshold. When the experimental pressure was increased to 22.4, 24.6, and 28.4 MPa, fully miscible displacement was achieved, with higher oil recovery factors of 91.28%, 93.34%, and 96.35%, respectively. Observations through the visual window further confirmed the characteristics of miscible flooding. The MMP was determined using the intersection of two linear fits, where three data points with recovery factors below 90% and three data points with recovery factors above 90% were fitted separately. The intersection of these two lines yielded an experimental MMP of 20.87 MPa. Additionally, the WinProp simulation predicted an MMP of 19.73 MPa, while a knowledge-guided intelligent model (Shen et al., 2023b) estimated 20.37 MPa. Both simulation and machine learning predictions closely match the experimental results, verifying the robustness of our MMP estimations in CCUS-EOR applications.

3.1.3. *Coreflooding experiments*

The coreflooding experiments were conducted to evaluate the oil recovery and CO_2 storage potential of miscible and non-miscible CO_2-WAG compared to continuous CO_2 injection. As shown in Fig. 8(a), CO_2-WAG significantly delayed gas breakthrough (from 1.37 to 1.84 PV), improved ultimate oil recovery (from 80.53% to 82.28%), and increased CO_2-enhanced oil recovery (from 25.69% to 29.85%) after water flooding. These improvements are attributed to the alternating injection of CO_2 and water, which suppresses viscous fingering and enhances sweep efficiency. Similarly, miscible CO_2-WAG outperformed non-miscible CO_2-WAG by further delaying breakthrough (from 1.67 to 1.84 PV) and increasing ultimate oil recovery (from 75.65% to 82.28%) as well as CO_2-enhanced oil recovery (from 26.89% to 29.85%) (Fig. 8(b)), highlighting the crucial role of miscibility in improving WAG performance.

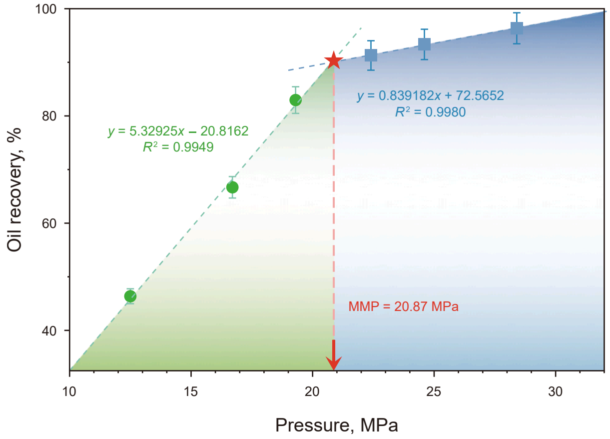

Fig. 7. Results of slim tube test. The green dashed line represents a linear fit through the three experimental points (green markers) with oil recovery factors below 90%, while the blue dashed line corresponds to the fit for the three points experimental (green markers) above 90%. The intersection of the two lines, marked by a red pentagram, indicates the MMP. Error bars represent a 3% experimental uncertainty.

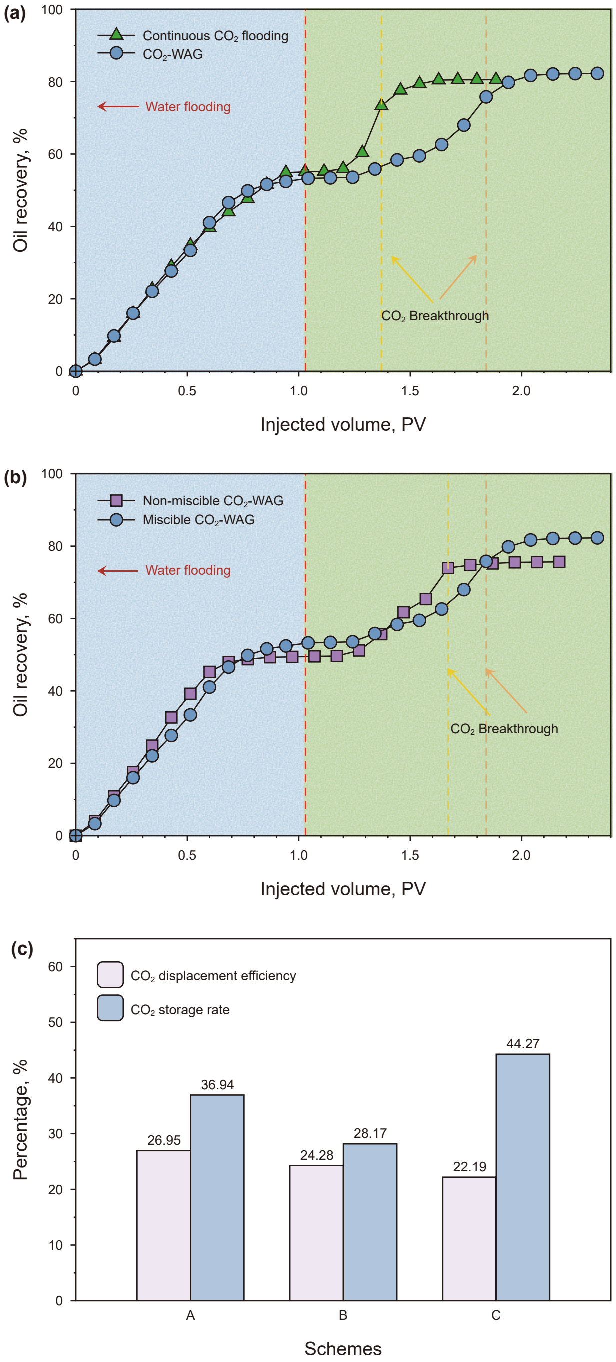

Fig. 8. Comparison of different long-core flooding experiments. **(a)** Continuous CO_2 injection vs. CO_2-WAG, **(b)** non-miscible CO_2-WAG vs. Miscible CO_2-WAG, **(c)** CO_2 displacement efficiency and CO_2 storage rate for three schemes: A (miscible CO_2-WAG), B (non-miscible CO_2-WAG), and C (continuous CO_2 injection).

To further compare CO_2 utilization and storage performance under three distinct injection strategies, two key indicators were evaluated: CO_2 storage rate, defined as the volume of retained CO_2 normalized by the pore volume, and CO_2 displacement efficiency, defined as the proportion of incremental oil recovery due to CO_2 injection, calculated as the volume of oil produced after waterflooding divided by the total volume of injected CO_2. As shown in Fig. 8(c), miscible CO_2-WAG achieved the highest CO_2 displacement efficiency (26.95%), outperforming non-miscible CO_2-WAG (24.28%) by 2.67%, highlighting the critical role of miscibility in enhancing oil recovery. Notably, non-miscible CO_2-WAG also demonstrated higher displacement efficiency than continuous CO_2 injection, which was performed under miscible conditions. This suggests that the injection strategy (i.e., WAG mode) may have a greater impact on CO_2 utilization than miscibility alone, as the alternating gas-water slugs can improve mobility control, delay gas breakthrough, and promote more effective sweep. This insight highlights the significance of injection design beyond fluid properties.

In terms of CO_2 storage, continuous CO_2 injection resulted in the highest CO_2 storage rate (44.27%), which is 7.33% higher than that of miscible CO_2-WAG (36.94%). This difference can be attributed to the pore volume being partially occupied by water in WAG processes, as well as the potential for CO_2 to dissolve into the water phase and be produced along with it. The additional pore space created by oil displacement is not sufficient to compensate for the CO_2 loss, leading to a relatively lower net storage in the WAG injection mode. This trade-off represents one of the main limitations of CO_2-WAG compared to continuous injection. However, it is often acceptable due to the superior displacement efficiency and economic returns provided by WAG, and it can be mitigated through optimized cycle design. Despite the slightly lower storage rate, miscible CO_2-WAG still achieved a favorable CO_2 storage rate (36.94%), significantly higher than that of non-miscible CO_2-WAG (28.17%), further emphasizing the dual importance of miscibility in enhancing both oil recovery and long-term CO_2 retention. These findings provide strong evidence for incorporating miscibility control in reservoir-scale numerical simulations. Moreover, the CO_2 storage rate observed under miscible CO_2-WAG conditions far exceeds typical values reported in previous literature, which are often below 20% (Li et al., 2021; Z. Li et al., 2022). This could be partially attributed to the relatively low total injection volume used in our experiments (0.7 PV), which helped mitigate early gas breakthroughs and facilitated better CO_2 confinement. Therefore, maintaining an optimal CO_2 injection volume is essential and offers valuable guidance for field-scale modeling and design. It is also worth noting that the waterflooding recovery remained comparable across all injection strategies, reaching approximately 50%–53% after 1 PV of water injection, ensuring a consistent baseline for evaluating CO_2 contributions. Additionally, both CO_2-WAG (seven alternating cycles totaling 0.7 PV of CO_2 and 0.7 PV of water) and continuous CO_2 injection were constrained to the same CO_2 volume (0.7 PV) for a fair comparison.

In summary, miscible CO_2-WAG presents itself as the most effective strategy, achieving a well-balanced performance between CO_2 utilization and storage. The WAG injection mode may play a more critical role than miscibility alone, as it enhances sweep efficiency and delays gas breakthrough. The only trade-off lies in the slight reduction of storage capacity caused by the presence of water slugs. This reduction is generally acceptable and can be further alleviated through optimized injection scheme design. These findings provide valuable guidance for the future design of operational parameters in CCUS-EOR applications.

3.2. Performance evaluation of CO_2-EOR and storage prediction models

We conducted five independent runs using different random seeds and an 80%–20% training-test split to ensure robustness in model evaluation. Hyperparameter tuning was performed using the widely adopted Bayesian optimization algorithm, Tree-structured Parzen Estimator (TPE) (Bergstra et al., 2011), combined with five-fold cross-validation. The computational budget for these runs ranged from 100 s to 3 h, depending on the complexity of each model's search space. All experiments were executed on a consumer-grade GPU (NVIDIA RTX 4070Ti), ensuring computational efficiency while maintaining reproducibility for practical applications. To ensure the physical consistency of model predictions, the TabPFN surrogate model was trained on simulation data generated from CO_2-WAG reservoir models that had been calibrated using mechanistic experimental observations, specifically incorporating experimentally derived fluid models. This approach not only guarantees high predictive accuracy but also ensures that the model faithfully captures fluid dynamics and displacement mechanisms consistent with those observed at the experimental scale.

To evaluate and compare the predictive performance of the TabPFN surrogate model against baseline models, we adopted four metrics: Root Mean Square Error (RMSE), Coefficient of Determination (R-squared, R^2), Mean Absolute Error (MAE), and Mean Absolute Percentage Error (MAPE). These metrics provide complementary perspectives on prediction accuracy by quantifying discrepancies between observations and predictions. Their specific formulations are detailed as follows:

$$\mathrm{RMSE} = \sqrt{\frac{1}{n}\sum_{i=1}^{n}(\widehat{y}_i - y_i)^2} \tag{10}$$

$$R^2 = 1 - \frac{\sum\limits_{i}(\widehat{y}_i - y_i)^2}{\sum\limits_{i}(\overline{y}_i - y_i)^2} \tag{11}$$

$$\mathrm{MAPE} = \frac{1}{n}\sum_{i=1}^{n}\left[\frac{|y_i - y_i|}{y_i}\right] \times 100 \tag{12}$$

$$\mathrm{MSE} = \frac{1}{n}\sum_{i=1}^{n}(y_i - \widehat{y}_i)^2 \tag{13}$$

where $\widehat{y}_i$ is the prediction of the i-th sample, y_i is the corresponding observation, and n is the number of samples.

Fig. 9 shows the comparison of TabPFN with the baseline models, averaging results across five repeated runs using different training-test splits at an 8:2 ratio with five random seeds. The baseline models include ridge regression (RG), random forest (RF), and multilayer perceptron (MLP), and eXtreme Gradient Boosting (XGBoost), representing commonly used classical linear, ensemble, neural network, and gradient-boosting approaches for tabular prediction, respectively. A detailed summary of their advantages and limitations is provided in Table S3 (Supplementary C) for reference. As shown in Fig. 9, RG, RF, and MLP exhibit significantly inferior performance across all four evaluation metrics compared to TabPFN, underscoring the limitations of shallow models. TabPFN outperforms XGBoost across all targets, achieving RMSE reductions of approximately 34.5%, 29.8%, and 22.5% (0.076, 0.059, 0.117 vs. XGBoost's 0.116, 0.084, 0.151) for cumulative oil production, CO_2 storage, and NPV, respectively. Likewise, it attains higher R^2 values (0.967, 0.972,

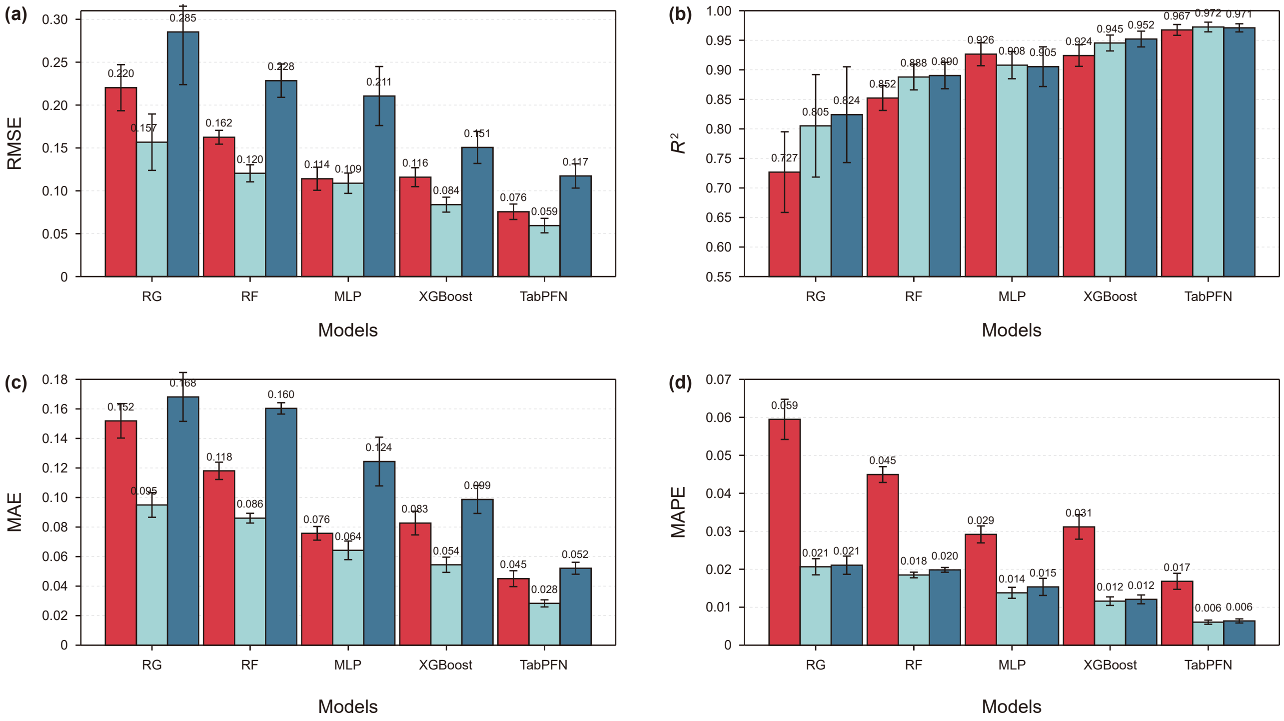

Fig. 9. Performance comparison of the TabPFN model with baseline models for all three targets across all four evaluation metrics: (red) Cumulative oil production (10^5 t), (light blue) CO_2 storage amount (10^6 t), and (blue) NPV (10^8 USD) across **(a)** RMSE, **(b)** R^2, **(c)** MAE, **(d)** MAPE. Error bars represent the average results over five repeated runs with different training-test splits (8:2 ratio) using varied random seeds.

0.971) compared to XGBoost (0.924, 0.945, 0.952). TabPFN also achieves significantly lower MAE (0.045, 0.028, 0.052) versus XGBoost (0.083, 0.054, 0.099), effectively halving absolute errors. Notably, TabPFN maintains prediction errors below 2% across all targets (MAPE: 1.7%, 0.6%, 0.6%), significantly lower than those of XGBoost (3.1%, 1.2%, 1.2%), thereby reinforcing its predictive accuracy and robustness. All models underwent identical hyperparameter tuning procedures to ensure fair comparison.

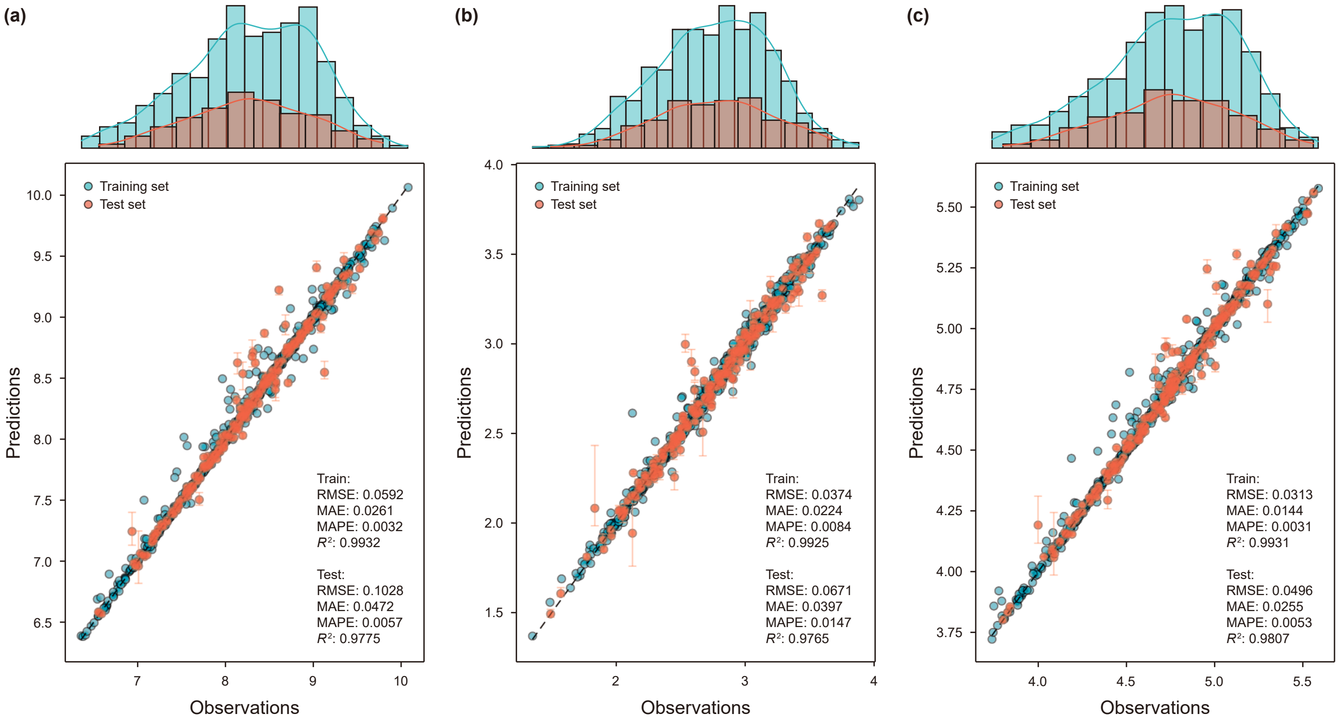

Fig. 10. Prediction performance of the TabPFN model for all three targets: **(a)** Cumulative oil production (10^5 t), **(b)** CO_2 storage amount (10^6 t), and **(c)** NPV (10^8 USD). The upper panels depict the distribution of train (light blue) and test (light red) data, while the lower panels present parity plots for model evaluation. Error bars represent the standard deviation of predictions across five repeated runs (using the same test set and varying training-validation splits at an 8:2 ratio with different random seeds).

We further evaluated the predictive performance of TabPFN on cumulative oil production, CO_2 storage capacity, and NPV through parity plots (Fig. 10). Both training and testing data points exhibit uniform distribution around the 45-degree parity line with minimal deviation, reflecting excellent fitting accuracy. Specifically, R^2 values of 0.9775, 0.9765, and 0.9807, alongside corresponding RMSEs of 0.1028, 0.0671, and 0.0496, confirm TabPFN's capacity to capture the underlying relationships between operational parameters and output targets. The short error bars observed over repeated runs further highlight the model's stability and robustness. Notably, the strong alignment between the predicted and actual extremes underscores TabPFN's outstanding OOD generalization capability. This characteristic is particularly crucial in CO_2-WAG modeling, where complex engineering design often cause distribution shifts between training data and real-world deployment. Moreover, TabPFN's excellent generalization strength enhances optimization reliability. Serving as a surrogate model, TabPFN significantly enhances the stability and predictive accuracy of optimization algorithms applied in CCUS-EOR operations. Its robust handling of diverse input distributions ensures consistent optimization outcomes, supporting practical CO_2 injection strategy design by reliably estimating both EOR potential and long-term CO_2 storage performance.

Despite its outstanding performance, several limitations have been identified. Specifically, the MAPE for CO_2 storage prediction (1.47%) is slightly higher than that of cumulative oil production (0.57%) and NPV (0.53%), indicating relatively higher prediction error. Conversely, cumulative oil production and NPV predictions, despite lower MAPE, show slightly larger deviations from the 45-degree parity line compared to CO_2 storage. Nevertheless, TabPFN demonstrates consistently superior overall predictive performance across all three targets. Future research could focus on further improving prediction fidelity by incorporating reservoir heterogeneity descriptors or integrating physics-informed constraints to enhance interpretability and accuracy in large-scale CCUS-EOR deployments.

In addition to its accuracy and generalization capability, TabPFN offers a significant computational speed advantage. Once trained, the model can predict system responses within a few seconds, compared to the 2–3 h typically required for each run of conventional reservoir simulations, resulting in a speedup of over 2000 times. Furthermore, TabPFN enables parallel predictions, making this acceleration even more pronounced in large-scale computing scenarios. For example, evaluating 1000 scenarios simultaneously can achieve a speed gain of 10^5–10^6 times, corresponding to five to six orders of magnitude acceleration. This remarkable acceleration enables large-scale optimization and real-time decision-making, which would be practically infeasible using traditional numerical simulations alone.

Overall, TabPFN's blend of high predictive accuracy, strong OOD generalization, model stability, and substantial computational speed advantage over traditional numerical methods makes it a powerful surrogate modeling tool for intelligent CO_2 injection strategy design and full-lifecycle evaluation of CCUS-EOR systems.

3.3. Feature importance interpretation using SHAP

In the large-scale deployment of CCUS-EOR applications, model interpretability is crucial for fostering engineers' trust and ensuring transparency. To demonstrate the interpretability of our model, we employ SHAP (SHapley Additive exPlanations) (Lundberg and Lee, 2017) to analyze feature importance. SHAP values quantify each feature's contribution to the model's output. The bar charts and beeswarm plots (Fig. 11) visualize the impact of individual features across all predictions. The definitions of all operational parameter abbreviations are provided in Supplementary D.

As shown in the bar charts (left panel of Fig. 11), GASI, GAS_TIME, WATER_TIME, and PRO_BHP emerge as the most influential parameters affecting all three objectives throughout the full-cycle CCUS-EOR. Fine-tuning these four parameters is critical for maximizing CO_2-EOR and storage performance. Overall, their relative importance is ranked as follows: GASI (0.49, 0.25, 0.25) > GAS_TIME (0.13, 0.12, 0.07) > WATER_TIME (0.12, 0.11, 0.07) > PRO_BHP (0.12, 0.06, 0.07) ≈ WATI (0.15, 0.04, 0.06). Notably, GASI exhibits the highest importance, with its impact on EOR and NPV nearly three times greater than other parameters, and twice as significant for CO_2 storage. The bee swarm plots (right panel of Fig. 11) further confirm that GASI and GAS_TIME are positively correlated with all objectives, while WATER_TIME and PRO_BHP show negative correlations. This shows that increasing the CO_2 injection rate and extending the gas injection time can significantly improve oil recovery efficiency and storage capacity. The physical mechanism of this phenomenon has been verified in multiple studies (Ghahfarokhi et al., 2016; Li et al., 2021). Higher GASI and longer GAS_TIME indicate larger CO_2 injection volumes and longer CO_2 cycles, increasing pore occupancy and increasing CO_2-oil contact area and interaction time, thereby improving both oil recovery and CO_2 storage capacity. Conversely, maintaining a relatively low PRO_BHP is essential for creating a favorable pressure differential, though it is typically set slightly above the MMP to ensure miscibility and stable gas-oil interactions (Ghahfarokhi et al., 2016). Similarly, a shorter WATER_TIME increases the ratio of gas to water injection within each cycle, optimizing the mobility ratio and delaying premature water breakthrough, which improves sweep efficiency. As confirmed in (Ghahfarokhi et al., 2016), longer CO_2 cycles and shorter water cycles enhance injectivity and pattern conformance. Interestingly, the water injection rate (WATI) shows a strong positive impact on oil recovery and NPV (importance scores of 0.15 and 0.06, respectively), but shows a slightly negative impact on CO_2 storage (importance score: 0.04). This agrees with prior research indicating that increased water injection rates raise reservoir pressure and facilitate water slug formation (Chen et al., 2020; Sampaio et al., 2020). This is because a higher water injection rate accelerates water slug formation, suppressing CO_2 channeling and improving sweep efficiency, thereby favoring oil production. However, it reduces available pore space for CO_2 storage. Excessive water injection rates may also elevate water cuts and hinder recovery (Chen et al., 2010). Our findings indicate that, under a fixed injection volume, prioritizing higher injection rates (GASI, WATI) is more effective than extending injection time (GAS_TIME, WATER_TIME). Specifically, elevating WATI while shortening WATER_TIME (as reflected by the blue cluster for WATER_TIME and red cluster for WATI in Fig. 11(a) and (c)) enhances both oil production and economic returns. Similarly, the shorter GAS_TIME values indicate that reducing gas injection time is beneficial for oil recovery. Therefore, under a fixed total injection volume, prioritizing higher injection rates over longer injection durations emerges as the optimal strategy. This finding highlights that, in the context of carbon neutrality goals, efficient CO_2 utilization and storage strategies should focus on maximizing instantaneous injection intensity rather than merely extending injection periods. For example, within a 20-year operational timeframe (e.g., by 2040), merely extending the injection duration is insufficient to offset the storage deficits caused by lower injection intensities. Achieving an equivalent storage capacity would require a significantly longer period (e.g., 31 years) (Xu et al., 2024).

Additionally, the model also correctly identifies that STG_INJ_STORAGE_WELL has negligible influence on oil recovery,

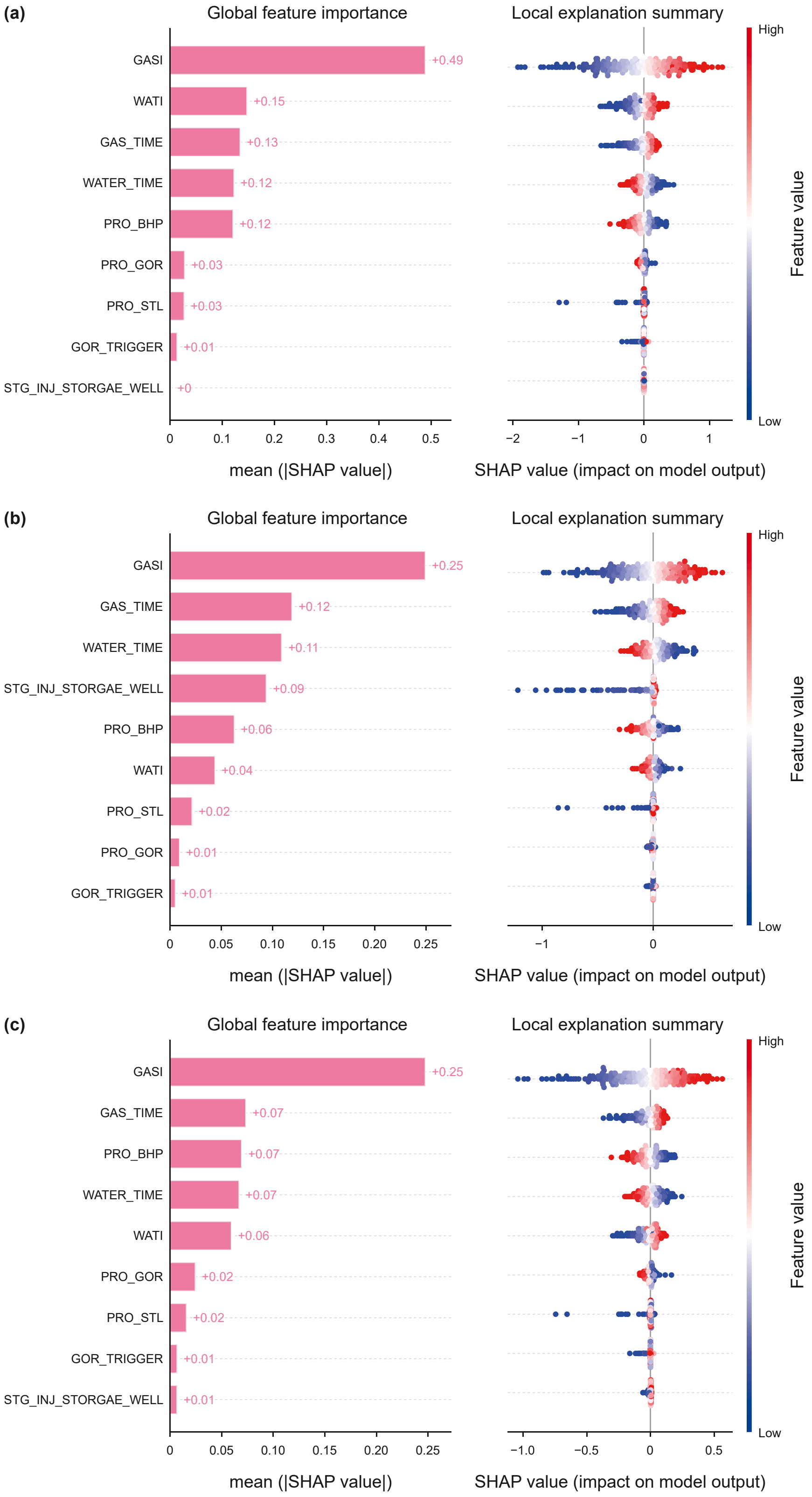

Fig. 11. Feature importance-based interpretability analysis across all three targets: **(a)** Cumulative oil production (10^5 t), **(b)** CO_2 storage amount (10^6 t), and **(c)** NPV (10^8 USD). The left panel shows bar plots of SHAP values for each feature, where longer bars indicate higher feature importance. The right panel presents beeswarm plots, where each point represents a WAG scheme, and its position along the *X*-axis reflects the impact of that feature on the model prediction for the corresponding scheme. The density of stacked points indicates the distribution of feature effects across all schemes.

which aligns with operational logic: CO_2 injection into storage wells requires shutting in production wells, meaning this parameter primarily affects storage rather than recovery. Similarly, the maximum total surface liquid production rate of production wells (PRO_STL) shows minimal influence across all objectives. Although production constraints are theoretically expected to affect recovery, this suggests that most PRO_STL values (around 55 for over 80% of the data) exceed the actual operational threshold, making further increases unnecessary and potentially cost-inefficient. This conclusion is consistent with prior findings showing that elevated PRO_STL values offer limited marginal gains (Sampaio et al., 2020). Furthermore, PRO_GOR (well-level gas-oil ratio limit) shows a greater influence than GOR_TRIGGER (field-level shutdown threshold). This indicates that fine-grained GOR control at the well level is more effective in mitigating gas breakthrough (Khanifar et al., 2025), eliminating the need for broad field-level controls (e.g. maximum GOR) (Sampaio et al., 2020). Lower PRO_GOR values (i.e., earlier well shutdowns) correlate with suppressed gas channeling and improved economic returns, while higher values support extended CO_2 injection and improved storage outcomes.

In summary, the proposed model robustly captures the importance of key operational parameters and their physical mechanisms, providing valuable insights into how these parameters jointly affect oil recovery, CO_2 storage, and economic performance in CCUS-EOR systems. These findings form a strong basis for multi-objective optimization and decision-making strategies in the pursuit of carbon neutrality goals.

3.4. Pareto front solutions via multi-objective optimization

The ACAM-NSGA-II algorithm was configured with a population size of 200, adaptive crossover ($k_1 = 1.4622$, $k_2 = 0.2293$) and mutation ($k_3 = 1.0867$, $k_4 = 0.8565$) operators, where the adaptive parameters were determined through random search optimization over 200 generations. Coupled with the TabPFN surrogate model, ACAM-NSGA-II successfully identified Pareto-optimal solutions across all three objectives considered in this study: oil recovery, CO_2 storage, and NPV. To facilitate clear interpretation, we primarily visualize the results in two dimensions, focusing on oil recovery versus CO_2 storage (Fig. 12), while NPV remains fully integrated into the optimization process. This 2D projection also facilitates a clear correspondence with the optimized time-series responses. The results confirm the algorithm's ability to efficiently and consistently construct high-quality Pareto fronts (Fig. 12(a)). Notably, all Monte Carlo simulation results are dominated by the Pareto-optimal solutions (Fig. 12(b)), further validating the quality and effectiveness of the generated Pareto front.

To ensure robustness and eliminate potential bias, the optimization was repeated five times with different random seeds. As shown in Fig. 12(c), ACAM-NSGA-II outperforms baseline algorithms (NSGA-II, NSGA-III, CTAEA, and R-NSGA-II) across all runs, with shaded regions representing standard deviations. ACAM-NSGA-II consistently achieved superior hypervolume values compared to all baselines. Interestingly, even the standard NSGA-II outperformed NSGA-III, CTAEA, and R-NSGA-II, likely due to its better balance between convergence and diversity preservation, which aligns well with the characteristics of CCUS-EOR optimization problems. The integration of adaptive crossover and mutation strategies further elevated performance, affirming the effectiveness of the proposed adaptive mechanisms. Moreover, convergence and stabilization were observed around generation 40 for all algorithms, reflecting the stability and reliability of the TabPFN surrogate model.

Fig. 13 presents the time-series profiles of oil production and CO_2 storage obtained by inputting the operational parameters of the Pareto-optimal solutions into CMG-GEM simulations for the maximum oil recovery and maximum CO_2 storage schemes. The Pareto-optimal solutions consistently outperformed all Monte Carlo cases in terms of oil production and CO_2 storage. Specifically, under the baseline scenario, oil production and storage capacity in the target block were projected to be depleted by around 2040, posing challenges for carbon neutrality targets. In contrast, the

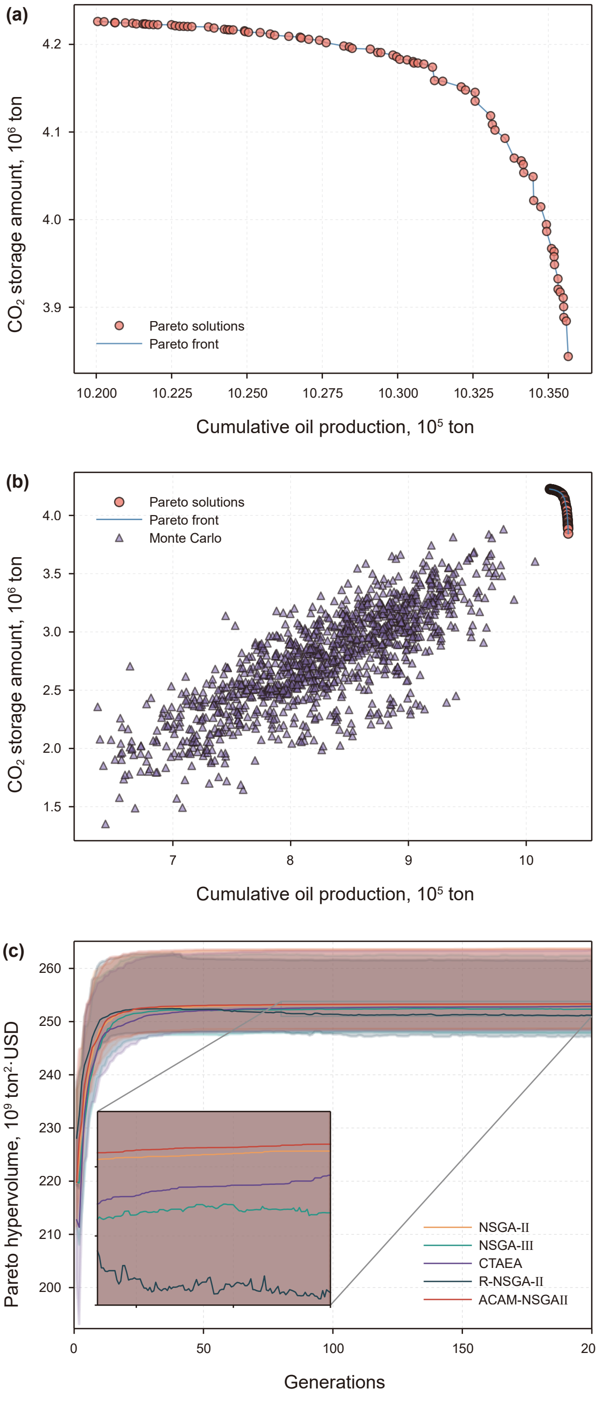

Fig. 12. Pareto front visualization and comparative analysis. **(a)** Pareto front shows the trade-off between cumulative oil production and CO_2 storage amount, **(b)** Pareto-optimal solutions (orange circles) on the Pareto front (blue lines) dominate the Monte Carlo simulation results (purple triangles), **(c)** hypervolume comparison between ACAM-NSGA-II and different optimization algorithms (NSGA-II, NSGA-III, CTAEA, and R-NSGA-II).

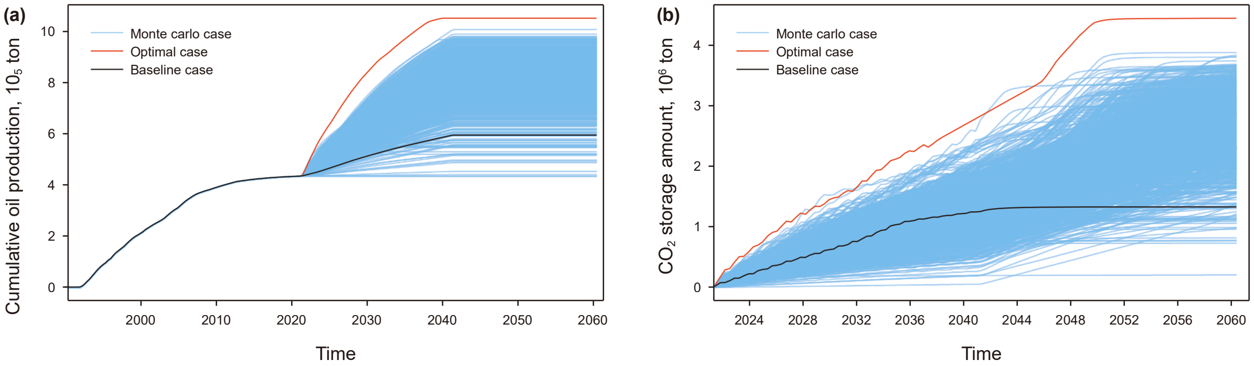

Fig. 13. Performance comparison of optimized cases, baseline cases, and Monte Carlo cases. Time series of **(a)** cumulative oil production and **(b)** CO$_2$ storage amount are generated for each case. The red solid lines represent the CMG-GEM simulation results under the optimal operational parameters derived from ACAM-NSGA-II for oil recovery and storage, respectively. The black and blue solid lines correspond to the baseline case and Monte Carlo cases, respectively.

optimized strategies effectively balance enhanced oil recovery with CO$_2$ storage goals. Specifically, the maximum cumulative oil production improved from 5.95×10^5 to 1.05×10^6 tons, raising the oil recovery factor from 35.17% to 62.22% (with geological reserves of 1.69 million tons); the maximum CO$_2$ storage volume increased from 1.33×10^6 to 4.45×10^6 tons, representing a more than 3.3-fold improvement; and NPV rose from \$344 million to \$578 million, corresponding to a ~68.0% enhancement compared to the baseline.

Further insights into the spatial performance improvements are illustrated in Fig. 14, which compare the oil saturation distributions for the baseline and maximum oil recovery scheme, along with the CO$_2$ saturation distribution from numerical simulations for the storage-maximizing scheme. Three key observations emerge: (1) The optimized solutions significantly enhanced oil recovery and CO$_2$ storage across nearly all reservoir layers, including the upper, middle, and lower layers, as evidenced by lower oil saturation and higher CO$_2$ saturation (Fig. 14(a)–(c)) and 14(d)–(f)); (2) Oil saturation reductions were more pronounced in the upper and middle layers compared to the lower layer. This can be attributed to the balanced design of WAG injection, which mitigates heterogeneity and high-permeability channeling, coupled with GOR-controlled shut-in strategies that prevent overproduction from highly depleted lower layers, ensuring more uniform recovery; (3) Under the optimized operational parameters, CO$_2$ storage in the lower layers increased most significantly. This can be explained by

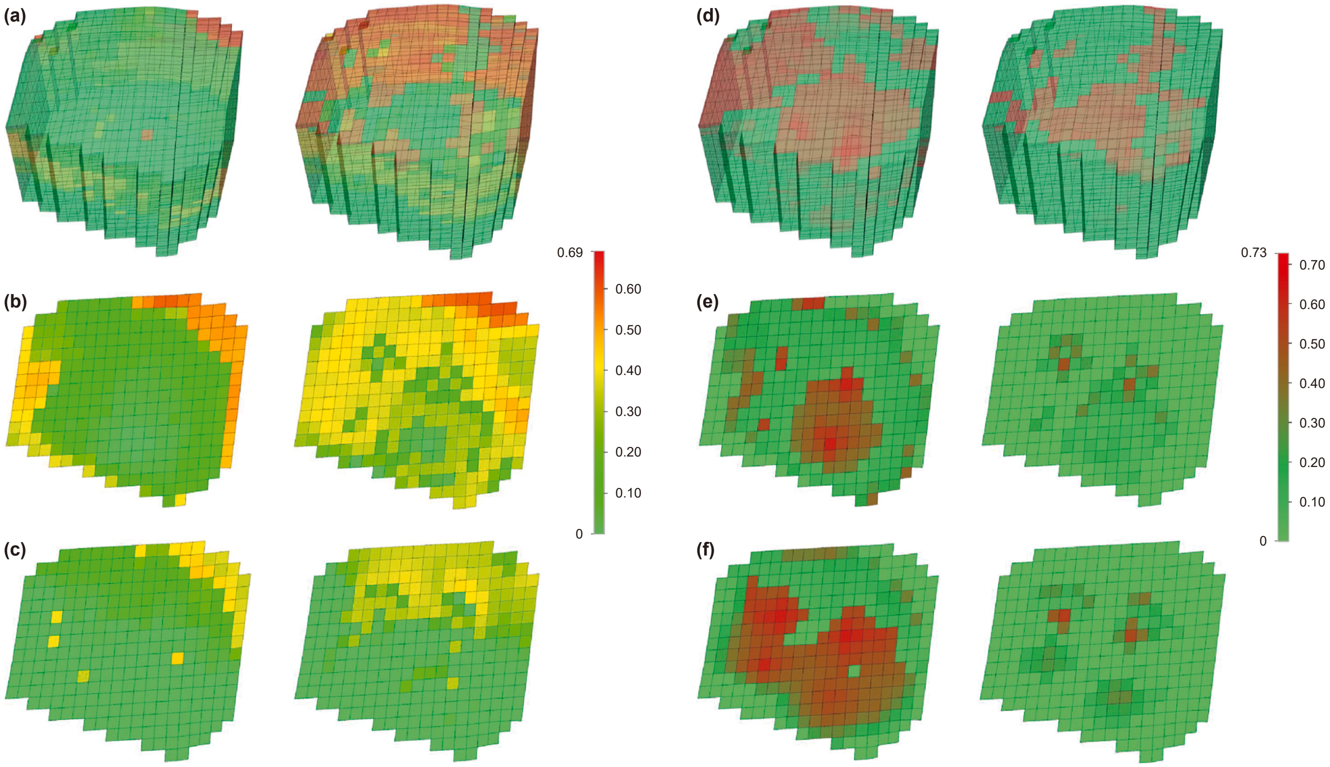

Fig. 14. Comparison of oil and gas saturation spatial distributions between the optimized (left) and baseline (right) scheme after 20 years of CO$_2$-WAG injection. The top, middle, and bottom rows correspond to the 3D view, the middle (12th), and the bottom (21st) layers, respectively, showing oil saturation **(a–c)** and gas saturation **(d–f)**.

sufficient CO_2 injection saturating the residual pore space in the upper and middle layers before accumulating heavily in the lower layers. These findings suggest that, under fracture pressure constraints, CO_2 storage capacity in the target block is nearing its theoretical upper limit across all feasible injection strategies.

3.5. Subdivision of Pareto solutions and interpretation of underlying mechanisms

To further analyze the Pareto front, we applied the K-means clustering algorithm to divide the solutions into three distinct regions: the high CO_2 storage zone (Cluster 0), the EOR-storage synergy zone (Cluster 1), and the high oil recovery zone (Cluster 2), as illustrated in Fig. 15(a). The clustering was performed based on comprehensive information for each solution sample, including operational parameters and not limited to the three objective variables (cumulative oil production, CO_2 storage amount, and NPV). This allowed us to capture the intrinsic similarities in operational characteristics across the Pareto front. For improved clarity and interpretability, the Pareto solutions are presented in 2D plots. Subsequently, we further quantified the distribution of key operational parameters within each cluster (Fig. 15(b)–(i)) to reveal the distinct operational strategies and underlying physical mechanisms associated with each zone.

The high CO_2 storage zone (Cluster 0) is characterized by a low WAG ratio (0.12) during the EOR stage, involving large-volume gas slug injection combined with limited water injection (low WATI and short WATER_TIME). Additionally, it features high gas injection rates (high GASI) but short gas injection time (short GAS_TIME), relatively low production well shut-in gas-oil ratios (PRO_GOR), and the highest CO_2 injection rates during the storage stage (STG_INJ_STORAGE_WELL). The operational strategy in this cluster prioritizes maximizing long-term CO_2 storage. Although the low WAG ratio increases CO_2 injection volumes, it also raises the risk of gas channeling. Together with the lower GOR thresholds and early well shut-in, hydrocarbon production is restricted, thereby reducing CO_2 recycling and enhancing its retention in the reservoir. The high CO_2 injection rate during the storage phase ensures that substantial amounts of CO_2 are injected post-EOR, fully utilizing the available pore space. Physically, Cluster 0 predominantly operates under near-miscible to immiscible conditions, where the interfacial tension between CO_2 and oil remains relatively high. The incomplete reduction of interfacial tension limits the increase of the capillary number, meaning that capillary forces still dominate over viscous forces within the pore system (Lake, 1989). As a result, CO_2 cannot effectively displace the trapped oil at the pore scale, leading to reduced microscopic displacement efficiency. Meanwhile, the strong capillary pressure and discontinuous gas connectivity promote residual CO_2 trapping within pore networks, while capillary entry pressure at the caprock interface contributes indirectly to structural containment by preventing upward CO_2 migration (Bachu, 2008; Pentland et al., 2011). Therefore, although oil recovery is compromised, this mechanism substantially enhances the long-term CO_2 storage

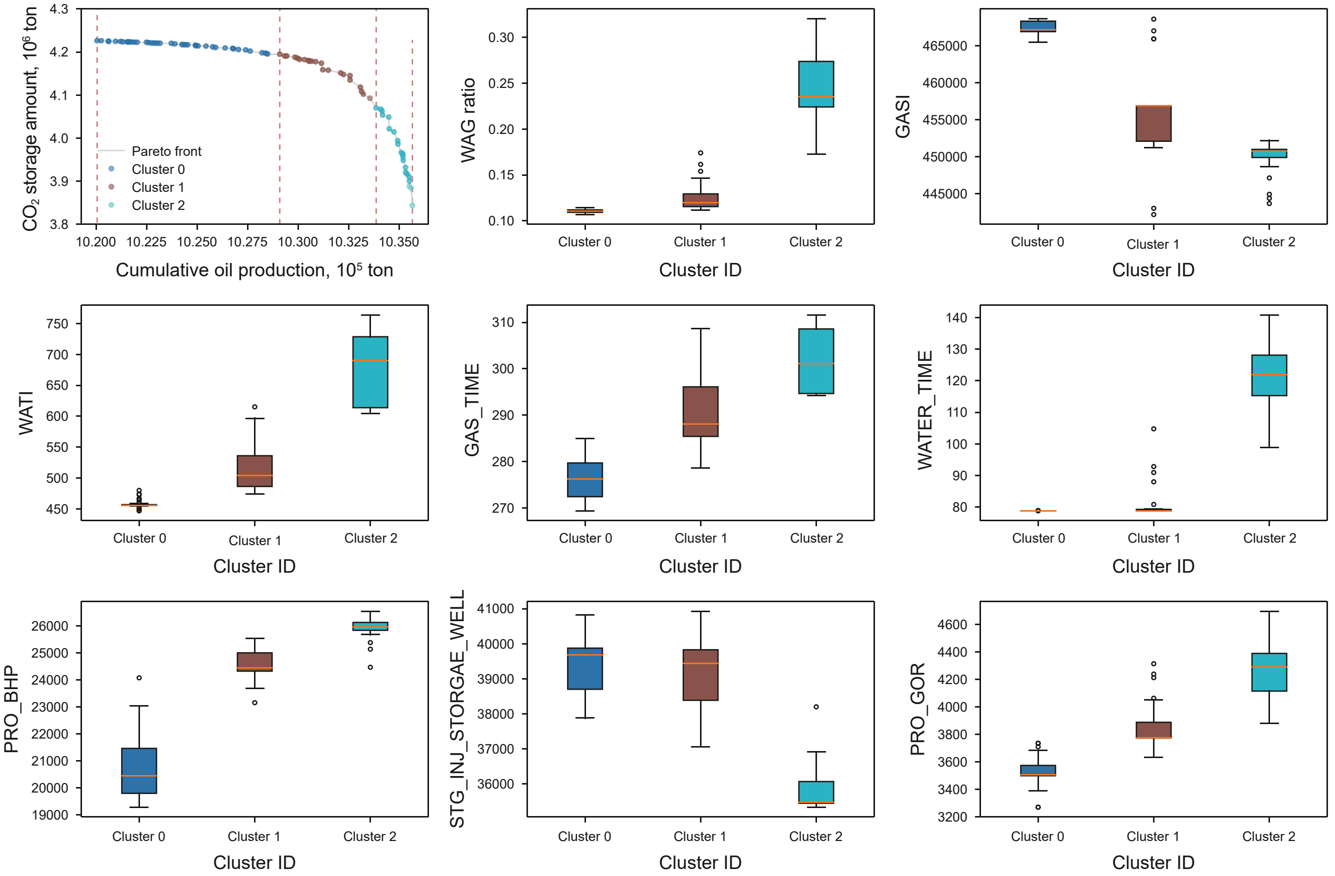

Fig. 15. Clustering-based subdivision of the Pareto front: trade-off analysis of operational strategies and physical mechanisms. **(a)** The Pareto front is clustered into three regions using the K-means algorithm: high CO_2 storage zone (Cluster 0, dark blue), balanced EOR-carbon zone (Cluster 1, brown), and high oil recovery zone (Cluster 2, light blue). **(b–i)** Boxplots showing the distribution of key operational parameters, including WAG ratio, GASI, WATI, GAS_TIME, WATER_TIME, PRO_BHP, STG_INJ_STORAGE_WELL, and PRO_GOR, across the three clusters.

efficiency of Cluster 0. While favorable for CO_2 dissolution and diffusion (Chen et al., 2022a), the residual interfacial forces limit oil swelling and displacement efficiency, explaining why oil recovery is lower in favor of maximizing storage.

The EOR-storage synergy zone (Cluster 1) exhibits intermediate values across all key operational parameters, reflecting a balanced optimization between oil recovery and CO_2 sequestration. Moderate gas and water injection rates and durations ensure effective oil displacement while maintaining a reasonable amount of CO_2 storage. This configuration establishes a miscible flooding regime under reservoir pressures slightly above MMP, where interfacial tension is significantly reduced and the capillary number is moderately enhanced. Under these conditions, CO_2 dissolves partially and diffuses into the crude oil, lowering its viscosity and residual saturation, while maintaining limited capillary barriers that help stabilize the CO_2 front. This transitional near-fully-miscible state allows both diffusion-driven mass transfer and capillary-controlled displacement to operate simultaneously, producing a synergistic balance between oil recovery and CO_2 storage. Furthermore, by appropriately adjusting the production well shut-in GOR limit (~3800 m^3/m^3) and storage-phase injection rate (~39,000 m^3/d), Cluster 1 achieves an optimized operational balance between mobility control and CO_2 retention, effectively mitigating gas channeling, sustaining reservoir pressure, and enhancing both recovery and long-term storage performance.

The high oil recovery zone (Cluster 2) exhibits the highest WAG ratio (approximately 0.25) during the EOR stage, characterized by large-volume gas and water slug injection, with relatively lower GASI and extended gas injection time (long GAS_TIME), higher water injection rates (high WATI), and longer water injection time (long WATER_TIME). It also displays higher production well shut-in GOR thresholds (PRO_GOR) and the lowest CO_2 injection rates during the storage stage. This cluster is focused on maximizing cumulative oil recovery. The combined injection of large water volumes and moderate CO_2 forms balanced slugs that effectively reduce gas channeling and suppress viscous fingering (He et al., 2023, 2024), thus stabilizing the displacement front, delaying gas breakthrough, and improving CO_2 sweep efficiency. Longer gas injection time (~300 days) ensures deeper penetration of the gas front, while extended water injection time (~700 days) effectively suppresses early gas breakthrough without excessive water production. It should be noted that although the GASI in this cluster is relatively lower compared to Cluster 0, the injection rate (~450,000 m^3/d) remains high. Critically, the elevated shut-in GOR threshold (~4300 m^3/m^3) allows for extended production phases, maximizing hydrocarbon recovery before well closure. The high oil recovery zone operates under fully miscible conditions at higher pressures (~26 MPa), significantly exceeding the MMP. Under these conditions, CO_2 dissolves completely in crude oil, causing pronounced oil swelling, viscosity reduction, and a nearly complete elimination of interfacial tension. These effects greatly enhance microscopic displacement efficiency and mobilize residual oil, leading to the highest oil recovery among all clusters (Kumar et al., 2022). However, the disappearance of distinct CO_2-oil interfaces also eliminates capillary barriers and discontinuous gas phase structures that are essential for residual and structural trapping. As a result, CO_2 tends to migrate continuously through the pore network and is more likely to be produced with the oil rather than immobilized within the formation. Consequently, long-term CO_2 retention capacity is limited, as the system favors enhanced displacement over storage stabilization. However, the lower CO_2 injection rates during the storage phase indicate a lower priority placed on post-EOR CO_2 storage, with operational focus concentrated on maximizing oil production.

In summary, each cluster reflects a distinct operational mode aligned with specific objectives: (1) Cluster 0 prioritizes CO_2 storage, characterized by early production shut-in, high storage-phase injection rates, and near-miscible conditions; (2) Cluster 1 balances oil recovery and storage by adjusting injection rates and time to optimize both; (3) Cluster 2 maximizes oil recovery through aggressive gas and water injection strategies and extended production, at the expense of CO_2 storage capacity. These findings highlight the inherent trade-offs in CCUS-EOR projects and provide valuable guidance for formulating operational strategies tailored to specific reservoir management goals. Importantly, this clustering analysis also reflects our integrated methodology that tightly couples experimental observations, reservoir simulations, and intelligent modeling. Specifically, the simulation data used for clustering and model training was derived from CO_2-WAG reservoir models calibrated using fluid property measurements and displacement behavior obtained from mechanistic laboratory experiments. This ensures that the identified cluster-specific operational strategies are not only statistically robust, but also grounded in physically validated mechanisms observed at the pore and core scale. The resulting patterns thus embody a cross-scale consistency from mechanism experiments through reservoir-scale simulation to surrogate modeling, greatly enhancing the interpretability and reliability of the findings.

4. Conclusions

In summary, we propose a highly generalizable, scalable, and efficient deep learning framework for the automated optimization of full-cycle CCUS-EOR injection strategies, achieving optimal trade-offs among oil recovery, CO_2 storage, and NPV without relying on expert knowledge or prior assumptions. The approach adopts a progressive workflow, where experimental measurements precisely characterize CO_2-oil property changes and microscale mechanisms, providing reliable references for simulation parameter design and ensuring physical consistency. The efficient TabPFN surrogate predictor achieves superior stability and accuracy (with an average R^2 of 0.97, RMSE of 0.084, and MAPE of 1%) compared to conventional baseline models. Coupled with the ACAM-NSGA-II algorithm, the framework identifies higher-quality Pareto fronts compared to traditional optimization approaches. Specifically, it enhances cumulative oil production from 5.95×10^5 to 1.05×10^6 t, increases CO_2 storage from 1.33×10^6 to 4.45×10^6 t, and boosts NPV from $344 million to $578 million. Further analysis using SHAP-based feature importance and k-means clustering reveals three representative Pareto-optimal solution patterns. The key operational parameters are ranked in importance as: GASI > GAS_TIME > WATER_TIME > PRO_BHP ≈ WATI. For a given total injection volume, prioritizing higher injection rates over prolonged injection durations is shown to be the optimal strategy for enhancing both oil recovery and CO_2 storage efficiency. Additionally, maintaining surface liquid production of production wells around 55 m^3/d and setting CO_2 injection rates during the CO_2 storage stage within 36,000–40000 m^3/d achieve high CO_2-EOR and storage performance while avoiding unnecessary production cost constraints. Furthermore, individual well-level GOR control proves more effective than field-level constraints, providing better mitigation of gas breakthrough without compromising overall operational efficiency. Overall, the proposed framework is not only well-suited for CCUS-EOR but also broadly applicable to petroleum engineering and wider energy systems involving complex parameter control and multi-objective decision-making. Its efficiency and scalability make it particularly valuable for large-scale, simulation-driven design tasks. Future research will extend this framework to more complex and heterogeneous reservoir conditions using larger-scale datasets to enhance model robustness and generalizability. Building upon the WAG foundation established in this study, future work will further incorporate additional physical and chemical mechanisms, such as fingering instability, wellbore heat loss, caprock integrity failure, and CO_2-water-rock interactions, and integrate these mechanistic insights into machine learning models to quantitatively evaluate their impacts on CCUS-EOR performance.

CRediT authorship contribution statement

Bin Shen: Writing – review & editing, Writing – original draft, Visualization, Methodology, Funding acquisition, Conceptualization. **Sheng-Lai Yang:** Writing – original draft, Supervision, Funding acquisition. **Yi-Qi Zhang:** Visualization, Validation, Methodology. **Xin-Yuan Gao:** Validation, Software, Methodology. **Lu-Fei Bi:** Software, Investigation. **Kai Du:** Methodology, Data curation. **Er-Meng Zhao:** Visualization, Validation. **Hong-Bo Zeng:** Writing – review & editing, Writing – original draft, Validation, Supervision, Methodology.

Declaration of competing interest

The authors declare that they have no known competing financial interests or personal relationships that could have appeared to influence the work reported in this paper.

Acknowledgements

This study is supported by the National Natural Science Foundation of China (Grant No. U23B2090 to Sheng-Lai Yang), the National Science Fund for Distinguished Young Scholars (Grant No. 52525403) and the National Key Research and Development Program of China (Grant No. 2023YFB4104204 to Sheng-Lai Yang).

Supplementary data

Supplementary data to this article can be found online at https://doi.org/10.1016/j.petsci.2026.01.028.

References

Abdelhafez, A., Alba, E., Luque, G., 2019. Performance analysis of synchronous and asynchronous distributed genetic algorithms on multiprocessors. Swarm Evol. Comput. 49, 147–157. https://doi.org/10.1016/j.swevo.2019.06.003.

Azzolina, N.A., Nakles, D.V., Gorecki, C.D., Peck, W.D., Ayash, S.C., Melzer, L.S., Chatterjee, S., 2015. CO_2 storage associated with CO_2 enhanced oil recovery: A statistical analysis of historical operations. Int. J. Greenh. Gas Control 37, 384–397. https://doi.org/10.1016/j.ijggc.2015.03.037.

Bachu, S., 2008. CO_2 storage in geological media: role, means, status and barriers to deployment. Prog. Energy Combust. Sci. 34, 254–273. https://doi.org/10.1016/j.pecs.2007.10.001.

Bergstra, J., Bardenet, R., Bengio, Y., Kégl, B., 2011. Algorithms for hyper-parameter optimization. In: Advances in Neural Information Processing Systems. Curran Associates, Inc., pp. 1–9

Chen, B., Pawar, R.J., 2019. Characterization of CO_2 storage and enhanced oil recovery in residual oil zones. Energy 183, 291–304. https://doi.org/10.1016/j.energy.2019.06.142.

Chen, B., Reynolds, A.C., 2016. Ensemble-based optimization of the water-alternating-gas-injection process. SPE J. 21, 786–798. https://doi.org/10.2118/173217-PA.

Chen, H., Liu, X., Zhang, C., Tan, X., Yang, R., Yang, S., Yang, J., 2022a. Effects of miscible degree and pore scale on seepage characteristics of unconventional reservoirs fluids due to supercritical CO_2 injection. Energy 239, 122287. https://doi.org/10.1016/j.energy.2021.122287.

Chen, H., Zhang, C., Yu, H., Wang, Z., Duncan, I., Zhou, X., Liu, X., Wang, Y., Yang, S., 2022b. Application of machine learning to evaluating and remediating models for energy and environmental engineering. Appl. Energy 320, 119286. https://doi.org/10.1016/j.apenergy.2022.119286.

Chen, M., Dai, J., Liu, X., Kuang, Y., Wang, Z., Gou, S., Qin, M., Li, M., 2020. Effect of displacement rates on fluid distributions and dynamics during water flooding in tight oil sandstone cores from nuclear magnetic resonance (NMR). J. Petrol. Sci. Eng. 184, 106588. https://doi.org/10.1016/j.petrol.2019.106588.

Chen, S., Li, H., Yang, D., Tontiwachwuthikul, P., 2010. Optimal parametric design for water-alternating-gas (WAG) process in a CO_2-Miscible flooding reservoir. J. Can. Petrol. Technol. 49, 75–82.

Christie, M., Eydinov, D., Demyanov, V., Talbot, J., Arnold, D., Shelkov, V., 2013. Use of multi-objective algorithms in history matching of a real field. In: All Days. Presented at the SPE Reservoir Simulation Symposium, SPE. https://doi.org/10.2118/163580-MS.

Deb, K., Pratap, A., Agarwal, S., Meyarivan, T., 2002. A fast and elitist multiobjective genetic algorithm: NSGA-II. IEEE Trans. Evol. Comput. 6, 182–197. https://doi.org/10.1109/4235.996017.

Dong, Q., Li, L., Dai, D., Zheng, C., Ma, J., Li, R., Xia, H., Xu, J., Wu, Z., Liu, T., Chang, B., Sun, X., Li, L., Sui, Z., 2024. A Survey on In-context Learning. https://doi.org/10.48550/arXiv.2301.00234.

Dou, L., Sun, L., Lyu, W., Wang, M., Gao, F., Gao, M., Jiang, H., 2023. Trend of global carbon dioxide capture, utilization and storage industry and challenges and countermeasures in China. Petrol. Explor. Dev. 50, 1246–1260. https://doi.org/10.1016/S1876-3804(23)60463-X.

Gao, X., Yang, S., Tian, L., Shen, B., Bi, L., Zhang, Y., Wang, M., Rui, Z., 2024. System and multi-physics coupling model of liquid-CO_2 injection on CO_2 storage with enhanced gas recovery (CSEGR) framework. Energy 294, 130951. https://doi.org/10.1016/j.energy.2024.130951.

Gao, X., Yang, S., Wang, B., Zhang, Y., Hu, J., Wang, M., Shen, B., Zhao, E., 2025. Pore-scale modeling of multiple fluids flow transport kinetics for CO_2 enhanced gas recovery. Energy 315, 134486. https://doi.org/10.1016/j.energy.2025.134486.

Ghahfarokhi, R.B., Pennell, S., Matson, M., Linroth, M., 2016. Overview of CO_2 injection and WAG sensitivity in SACROC. In: SPE Improved Oil Recovery Conference. SPE, Tulsa, Oklahoma, USA. https://doi.org/10.2118/179569-MS.

Han, Y.M., Park, C., Kang, J.M., 2010. Estimation of future production performance based on multi-objective history matching in a waterflooding project. In: The SPE EUROPEC/EAGE Annual Conference and Exhibition. OnePetro. https://doi.org/10.2118/130500-MS.

He, L., Ren, S., Zhang, H., 2023. Fingering crossover and enhanced oil recovery mechanism of water-alternating-CO_2 injection. Phys. Fluids 35, 053322. https://doi.org/10.1063/5.0150075.

He, L., Zhao, F.Y., He, W.J., Ren, S.K., Lou, R., Song, B.Y., 2024. Fingering inhibition triggered by CO_2 dissolution and viscosity reduction in water-alternating-CO_2 injection. Int. J. Heat Fluid Flow 110, 109646.

Hollmann, N., Müller, S., Purucker, L., Krishnakumar, A., Körfer, M., Hoo, S.B., Schirrmeister, R.T., Hutter, F., 2025. Accurate predictions on small data with a tabular foundation model. Nature 637, 319–326. https://doi.org/10.1038/s41586-024-08328-6.

Holm, L.W., 1982. CO_2 flooding: Its time has come. J. Petrol. Technol. 34, 2739–2745. https://doi.org/10.2118/11592-PA.

Hospedales, T., Antoniou, A., Micaelli, P., Storkey, A., 2022. Meta-learning in neural networks: A survey. IEEE Trans. Pattern Anal. Mach. Intell. 44, 5149–5169. https://doi.org/10.1109/TPAMI.2021.3079209.

Kamali, F., Hussain, F., Cinar, Y., 2017. An experimental and numerical analysis of water-alternating-gas and simultaneous-water-and-gas displacements for carbon dioxide enhanced oil recovery and storage. SPE J. 22, 521–538. https://doi.org/10.2118/183633-PA.

Khanifar, A., Panuganti, S.R., B Ibrahim, M.I.I., Sabri, M.N., B Rozali, M.I., Yusof, A.M., Motaei, E., Myo Thant, M.M., 2025. A novel AI-Based iGOR technology for real-time GOR control: a case study pilot plan for an enhanced oil rim reservoir management. In: The International Petroleum Technology Conference, IPTC. Kuala Lumpur, Malaysia. D012S003R008.

Kumar, N., Augusto Sampaio, M., Ojha, K., Hoteit, H., Mandal, A., 2022. Fundamental aspects, mechanisms and emerging possibilities of CO_2 miscible flooding in enhanced oil recovery: A review. Fuel 330, 125633. https://doi.org/10.1016/j.fuel.2022.125633.

Lake, L.W., 1989. Enhanced Oil Recovery. Prentice Hall, Englewood Cliffs, NJ.

LeCun, Y., Bengio, Y., Hinton, G., 2015. Deep learning. Nature 521, 436–444. https://doi.org/10.1038/nature14539.

Li, D., Saraji, S., Jiao, Z., Zhang, Y., 2021. CO_2 injection strategies for enhanced oil recovery and geological sequestration in a tight reservoir: an experimental study. Fuel 284, 119013. https://doi.org/10.1016/j.fuel.2020.119013.

Li, H., Gong, C., Liu, S., Xu, J., Imani, G., 2022a. Machine learning-assisted prediction of oil production and CO_2 storage effect in CO_2-Water-Alternating-Gas injection (CO2-WAG). Appl. Sci. 12, 10958. https://doi.org/10.3390/app122110958.

Li, Z., Su, Y., Li, L., Hao, Y., Wang, W., Meng, Y., Zhao, A., 2022b. Evaluation of CO_2 storage of water alternating gas flooding using experimental and numerical simulation methods. Fuel 311, 122489. https://doi.org/10.1016/j.fuel.2021.122489.

Liu, B., Yao, J., Sun, T., 2023. Numerical analysis of water-alternating-CO_2 flooding for CO_2-EOR and storage projects in residual oil zones. Int. J. Coal Sci. Technol. 10, 73. https://doi.org/10.1007/s40789-023-00647-9.

Liu, Z., Deng, Z., Davis, S., Ciais, P., 2023. Monitoring global carbon emissions in 2022. Nat. Rev. Earth Environ. 4, 205–206. https://doi.org/10.1038/s43017-023-00406-z.

Liu, Z., Liang, Y., Wang, Q., Guo, Y., Gao, M., Wang, Z., Liu, W., 2020. Status and progress of worldwide EOR field applications. J. Petrol. Sci. Eng. 193, 107449. https://doi.org/10.1016/j.petrol.2020.107449.

Lundberg, S.M., Lee, S.-I., 2017. A unified approach to interpreting model predictions. In: Proceedings of the 31st International Conference on Neural Information Processing Systems, NIPS'17. Curran Associates Inc., Red Hook, NY, USA, pp. 4768–4777.

Martin, D.F., Taber, J.J., 1992. Carbon dioxide flooding. J. Petrol. Technol. 44, 396–400. https://doi.org/10.2118/23564-PA.

Meinshausen, M., Meinshausen, N., Hare, W., Raper, S.C.B., Frieler, K., Knutti, R., Frame, D.J., Allen, M.R., 2009. Greenhouse-gas emission targets for limiting global warming to 2 °C. Nature 458, 1158–1162. https://doi.org/10.1038/nature08017.

Melzer, L.S., 2012. Carbon dioxide enhanced oil recovery (CO_2 EOR): factors involved in adding carbon capture, utilization and storage (CCUS) to enhanced oil recovery. Center for Climate and Energy Solutions 1–17.

Müller, S., Hollmann, N., Arango, S.P., Grabocka, J., Hutter, F., 2024. Transformers Can Do Bayesian Inference. https://doi.org/10.48550/arXiv.2112.10510.

Nagler, T., 2023. Statistical Foundations of Prior-Data Fitted Networks. https://doi.org/10.48550/arXiv.2305.11097.

Peng, G., Wu, Y., Zhang, C., Shen, W., 2021. Integrated optimization of storage location assignment and crane scheduling in an unmanned slab yard. Comput. Ind. Eng. 161, 107623. https://doi.org/10.1016/j.cie.2021.107623.

Pentland, C.H., El-Maghraby, R., Iglauer, S., Blunt, M.J., 2011. Measurements of the capillary trapping of super-critical carbon dioxide in Berea sandstone. Geophys. Res. Lett. 38. https://doi.org/10.1029/2011GL046683.

Pereira, F.G.A., Botechia, V.E., Schiozer, D.J., 2022. Model-based optimization of cycles of CO_2 water-alternating-gas (CO_2-WAG) injection in carbonate reservoir. BJPG 15, 139–149. https://doi.org/10.5419/bjpg2021-0012.

Ren, B., Male, F., Duncan, I.J., 2022. Economic analysis of CCUS: accelerated development for CO_2 EOR and storage in residual oil zones under the context of 45Q tax credit. Appl. Energy 321, 119393. https://doi.org/10.1016/j.apenergy.2022.119393.

Rui, Z., Liu, T., Wen, X., Meng, S., Li, Y., Dindoruk, B., 2025. Investigating the synergistic impact of CCUS-EOR. Engineering 48, 16–40. https://doi.org/10.1016/j.eng.2025.04.005.

Safarzadeh, M.A., Motahhari, S.M., 2014. Co-optimization of carbon dioxide storage and enhanced oil recovery in oil reservoirs using a multi-objective genetic algorithm (NSGA-II). Pet. Sci. 11, 460–468. https://doi.org/10.1007/s12182-014-0362-1.

Sampaio, M.A., De Mello, S.F., Schiozer, D.J., 2020. Impact of physical phenomena and cyclical reinjection in miscible CO_2-WAG recovery in carbonate reservoirs. J. Pet. Explor. Prod. Technol. 10, 3865–3881. https://doi.org/10.1007/s13202-020-00925-1.

Shen, B., Yang, S., Gao, X., Li, S., Ren, S., Chen, H., 2023a. A novel CO_2-EOR potential evaluation method based on BO-LightGBM algorithms using hybrid feature mining. Geoenergy Sci. Eng. 222, 211427. https://doi.org/10.1016/j.geoen.2023.211427.

Shen, B., Yang, S., Gao, X., Li, S., Yang, K., Hu, J., Chen, H., 2023b. Interpretable knowledge-guided framework for modeling minimum miscible pressure of CO_2-oil system in CO_2-EOR projects. Eng. Appl. Artif. Intell. 118, 105687. https://doi.org/10.1016/j.engappai.2022.105687.

Shen, B., Yang, S., Hu, J., Zhang, Y., Zhang, L., Ye, S., Yang, Z., Yu, J., Gao, X., Zhao, E., 2024. Interpretable causal-based temporal graph convolutional network framework in complex spatio-temporal systems for CCUS-EOR. Energy 309, 133129. https://doi.org/10.1016/j.energy.2024.133129.

Solomon, S., Plattner, G.-K., Knutti, R., Friedlingstein, P., 2009. Irreversible climate change due to carbon dioxide emissions. Proc. Natl. Acad. Sci. USA 106, 1704–1709. https://doi.org/10.1073/pnas.0812721106.

Song, X., Wang, F., Ma, D., Gao, M., Zhang, Y., 2023. Progress and prospect of carbon dioxide capture, utilization and storage in CNPC oilfields. Petrol. Explor. Dev. 50, 229–244. https://doi.org/10.1016/S1876-3804(22)60383-5.

Song, Y., Song, Z., Chen, Z., Mo, Y., Zhou, Q., Tian, S., 2024. Simulation of CO_2 enhanced oil recovery and storage in shale oil reservoirs: unveiling the impacts of nano-confinement and oil composition. Advances in Geo-Energy Research 13, 106–118. https://doi.org/10.46690/ager.2024.08.05.

Vaswani, A., Shazeer, N., Parmar, N., Uszkoreit, J., Jones, L., Gomez, A.N., Kaiser, Ł., Polosukhin, I., 2017. Attention is all you need. In: Proceedings of the 31st International Conference on Neural Information Processing Systems. Curran Associates, Inc., pp. 6000–6010

Wang, Y., Chu, H., Lyu, X., 2024. Deep learning in CO_2 geological utilization and storage: Recent advances and perspectives. Adv. Geo-Energy Res. 13, 161–165. https://doi.org/10.46690/ager.2024.09.01.

Wei, Y.M., Kang, J.N., Liu, L.C., Li, Q., Wang, P.T., Hou, J.J., Liang, Q.M., Liao, H., Huang, S.F., Yu, B., 2021. A proposed global layout of carbon capture and storage in line with a 2 °C climate target. Nat. Clim. Change 11, 112–118. https://doi.org/10.1038/s41558-020-00960-0.

Xiao, Z., Shen, B., Yang, J., Yang, K., Zhang, Y., Yang, S., 2024. Deep learning framework for accurate static and dynamic prediction of CO_2 enhanced oil recovery and storage capacity. Processes 12, 1693. https://doi.org/10.3390/pr12081693.

Xu, J., Wan, H., Wu, Y., Liu, S., Yan, B., 2024. Study on CO_2-Enhanced oil recovery and storage in near-depleted edge–bottom water reservoirs. JMSE 12, 2065. https://doi.org/10.3390/jmse12112065.

Yang, K., Yang, S., Hu, J., Gao, Y., Liu, X., Xiao, Z., 2024. Research on component variation and factors affecting minimum miscible pressure in low viscosity oil miscibility process. ACS Omega 9, 30131–30141. https://doi.org/10.1021/acsomega.3c08088.

Yi, J.H., Deb, S., Dong, J., Alavi, A.H., Wang, G.G., 2018. An improved NSGA-III algorithm with adaptive mutation operator for big data optimization problems. Future Gener. Comput. Syst. 88, 571–585. https://doi.org/10.1016/j.future.2018.06.008.

You, J., Ampomah, W., Sun, Q., 2020a. Co-optimizing water-alternating-carbon dioxide injection projects using a machine learning assisted computational framework. Appl. Energy 279, 115695. https://doi.org/10.1016/j.apenergy.2020.115695.

You, J., Ampomah, W., Sun, Q., 2020b. Development and application of a machine learning based multi-objective optimization workflow for CO_2-EOR projects. Fuel 264, 116758. https://doi.org/10.1016/j.fuel.2019.116758.

Yuan, S., Ma, D., Li, J., Zhou, T., Ji, Z., Han, H., 2022. Progress and prospects of carbon dioxide capture, EOR-utilization and storage industrialization. Petrol. Explor. Dev. 49, 955–962. https://doi.org/10.1016/s1876-3804(22)60324-0.

Zhang, N., Yin, M., Wei, M., Bai, B., 2019. Identification of CO_2 sequestration opportunities: CO_2 miscible flooding guidelines. Fuel 241, 459–467. https://doi.org/10.1016/j.fuel.2018.12.072.

Zhang, Y., Yang, S., Luo, Y., Han, Y., Tian, L., Liu, Q., Gao, X., Shen, B., Yang, R., Li, J., 2025. Visual characterization, exergy and mechanism analysis of in-situ nonequilibrium dynamic phase-behavior of CO_2-oil. Energy 328, 136560. https://doi.org/10.1016/j.energy.2025.136560.

Zhang, Y.Q., Yang, S.L., Bi, L.F., Gao, X.Y., Shen, B., Hu, J.T., Luo, Y., Zhao, Y., Chen, H., Li, J., 2024. A technical review of CO_2 flooding sweep-characteristics research advance and sweep-extend technology. Pet. Sci. 22 (1), 255–276. https://doi.org/10.1016/j.petsci.2024.09.005.

Zhou, X., Yu, W., Lei, G., Khan, S.Z., Al-Abdrabainabi, R., Kamal, M.S., Wu, Y.S., 2024. Experimental study on dual benefits of improvement of CO_2 enhanced oil recovery and its storage capacity for depleted carbonate oil reservoirs. Advances in Geo-Energy Research 12, 52–65. https://doi.org/10.46690/ager.2024.04.05.

Zhuang, X.Y., Wang, W.D., Su, Y.L., Li, Y., Li, L., Hao, Y.M., 2024. Co-optimization of CO_2-EOR strategies considering the spatio-temporal sequence prediction of CO_2 flooding and sequestration. In: The SPE Improved Oil Recovery Conference, SPE, Tulsa, Oklahoma, USA. https://doi.org/10.2118/218284-MS.